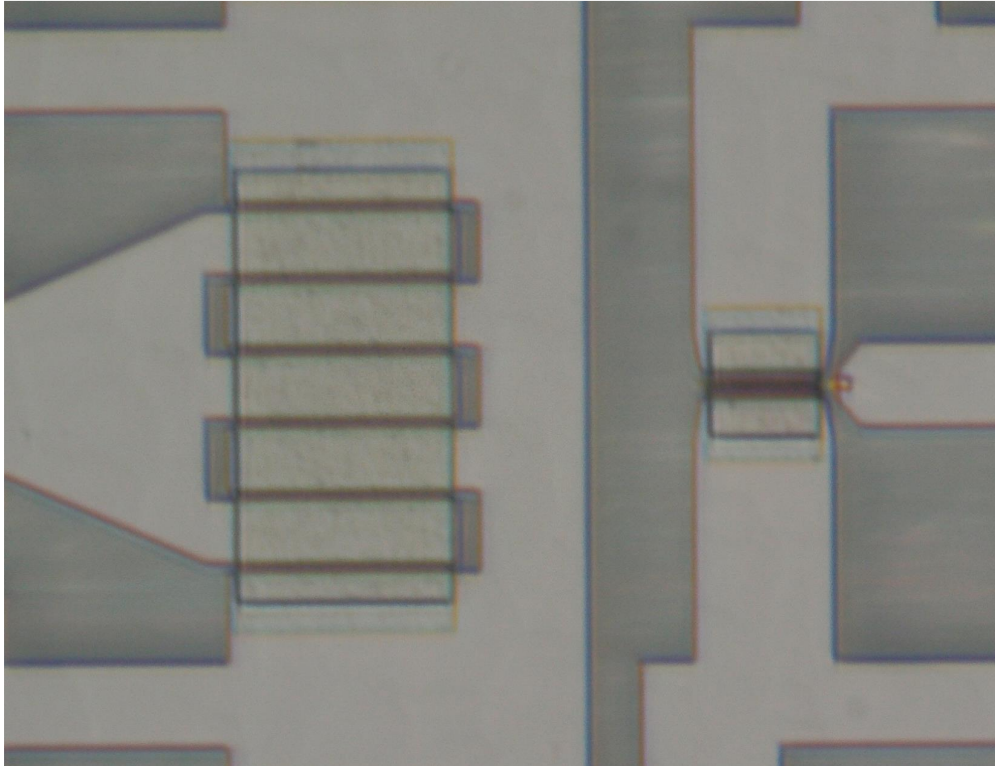




**CHALMERS**  
UNIVERSITY OF TECHNOLOGY

---



# Compensation of Thermal Effects by Dynamic Bias in Low Noise Amplifiers

Master's thesis in Wireless, Photonics and Space Engineering

JOHAN BREMER



MASTER'S THESIS 2017

# Compensation of Thermal Effects by Dynamic Bias in Low Noise Amplifiers

JOHAN BREMER



**CHALMERS**  
UNIVERSITY OF TECHNOLOGY

Department of Microtechnology and Nanoscience  
*Microwave Electronics Laboratory*  
CHALMERS UNIVERSITY OF TECHNOLOGY  
Gothenburg, Sweden 2017

Compensation of Thermal Effects by Dynamic Bias in Low Noise Amplifiers

JOHAN BREMER

© JOHAN BREMER, 2017.

Manager: Johan Carlert, Saab Technologies

Examiner: Niklas Rorsman, Department of Microtechnology and Nanoscience

Supervisor: Mattias Thorsell, Department of Microtechnology and Nanoscience

Supervisor: Torbjörn Nilsson, Saab Technologies

Master's Thesis 2017

Department of Microtechnology and Nanoscience

Microwave Electronics Laboratory

Chalmers University of Technology

SE-412 96 Gothenburg

Telephone +46 31 772 1000

Cover: A schottky diode placed 50  $\mu\text{m}$  to the right of a large mesa resistor.

Typeset in L<sup>A</sup>T<sub>E</sub>X

Gothenburg, Sweden 2017

## Abstract

There is an increasing need to understand how thermal effects affect the performance of amplifiers in radar systems. Increased chip power densities are to be expected as the integration of multiple transceivers in SiGe/BiCMOS and in GaN, increases. This will increase the electrical as well as thermal coupling between the transceivers, and the increased temperature is likely to impair the performance of amplifiers. Dynamic bias techniques are used today to increase the efficiency of transmitters. Therefore, it is important to investigate if these techniques can be used also to compensate for thermal effects which affect the elements in a multi transceiver chip. This thesis deals with the development of a GaN based temperature sensor as well as a study of the heat propagation properties in GaN on SiC structures. Furthermore, a study of thermal effects in low noise amplifiers has been carried out, and the use of dynamic bias to compensate for thermal performance deterioration, as well as other features, is demonstrated.

A mesa resistor sensor and Schottky diode sensor were designed and evaluated. It was shown that a 15  $\mu\text{m}$  mesa resistor works well as a temperature sensor when biased at an appropriate point. Models for predicting the temperature were developed based on measurements and a calibration method is proposed. It was shown that heat pulses can be detected by the sensors. A sensor area was designed and used to study heat propagation versus distance and temperature. A model describing the response of the sensor was proposed and evaluated. The model was used to study how heat is coupled to the sensor in the GaN and SiC layers. The thermal conductivity was seen to increase significantly in the GaN and SiC layers at lower temperatures. The layer time constants and propagation delay were observed to increase with temperature and distance. Light sources were also observed to impact the sensor current response.

It was determined by measurements that thermal effects in general degrades the performance of three evaluated low noise amplifiers, and that dynamic bias control techniques can be used to cancel these effects for certain parameters. Increased power consumption levels was observed when applying dynamic bias control. In addition, it was demonstrated how dynamic bias can be used to eliminate gain recovery effects after high power pulses. Lastly, suggestions for different modes of operation, where dynamic bias is utilized differently, are presented.

**Keywords:** GaN, LNA, dynamic bias, temperature sensor, thermal effects, thermal degradation, heat transfer, heat coupling, mesa, Schottky diode, modeling.



## Acknowledgements

I would like to thank the manager at Saab Technologies Johan Carlert who gave me the opportunity to work with this project in his group. Special thanks to my supervisor Mattias Thorsell at the Department of Microtechnology and Nanoscience who formulated and presented this project. He has been very engaged and enthusiastic about the work and his supervision has been very helpful and frequent. Thanks also to my supervisor Torbjörn Nilsson at Saab Technologies.

In addition, I would like to thank the personnel at the Microwave Electronics Laboratory who have assisted with practical issues, data analysis and modeling. Special thanks to Johan Bergsten who handled the processing of the GaN devices, Sebastian Gustafsson who helped solving problems related to the measurement setups and Lowisa Hanning who helped with modeling. Finally I would like to thank the people in the OEDWTA group at Saab Technologies who were involved in my project.

Johan Bremer, Gothenburg, June 2017





# Contents

<b>1</b>	<b>Introduction</b>	<b>1</b>
1.1	Thermal Challenges in GaN/SiGe BiCMOS . . . . .	1
1.2	Dynamic Bias Control . . . . .	2
1.3	Purpose of Study and Report Structure . . . . .	5
<b>2</b>	<b>GaN Temperature Sensor Study</b>	<b>7</b>
2.1	Sensor Design . . . . .	7
2.1.1	First Design Run . . . . .	7
2.1.2	Second Design Run . . . . .	9
2.2	Measurement Setup . . . . .	12
2.3	IV Measurements . . . . .	15
2.3.1	First Design Run . . . . .	15
2.3.2	Second Design Run . . . . .	16
2.4	Pulsed Measurements . . . . .	17
2.4.1	Distance Dependence . . . . .	17
2.4.2	Temperature Dependence . . . . .	21
2.5	Modeling . . . . .	23
2.5.1	Current Response . . . . .	23
2.5.2	IV Characteristics . . . . .	27
2.5.3	Temperature Estimation . . . . .	30
<b>3</b>	<b>Low Noise Amplifier Study</b>	<b>31</b>
3.1	Performance Parameters . . . . .	31
3.1.1	Noise Figure . . . . .	31
3.1.2	P1dB and Gain . . . . .	32
3.1.3	OIP3 . . . . .	34
3.2	Measurement Setup . . . . .	35
3.2.1	DUT Specifications and Settings . . . . .	37
3.3	Measurement Results . . . . .	39
3.3.1	IV Curves . . . . .	39
3.3.2	Bias Point Dependence . . . . .	41
3.3.3	Temperature Dependence . . . . .	46
3.3.4	Temperature and Bias Dependence . . . . .	50
3.3.4.1	Dynamic Bias Demonstration . . . . .	52
3.4	RF Pulse Measurement . . . . .	54

<b>4 Summary and Conclusions</b>	<b>57</b>
<b>5 Future Work</b>	<b>61</b>

# 1

## Introduction

Future highly integrated active antenna systems for sensors as well as communication systems will have more densely packed transceiver front-ends, with multiple transceivers on a single chip. This will increase the electrical as well as thermal coupling between the different functional blocks, such as power amplifiers and low noise amplifiers. The operating temperature of an amplifier is directly related to the electron mobility, and hence the current through the transistor. An increase in operating temperature will therefore directly impair the performance of the amplifier. Future systems will also have an increased demand for flexible operation. The communication industry demands flexible control of amplifiers to ensure maximum efficiency and linearity when operating with complex modulation signals. In radar applications, different operation scenarios demands adaptive control of receivers/-transmitters in order to maintain/enhance performance of the radar.

### 1.1 Thermal Challenges in GaN/SiGe BiCMOS

In the communication and radar industry, the development moves towards Multiple Input Multiple Output (MIMO) systems which includes multiple antennas for the transceiver front-ends. These MIMO systems provide spatial diversity and beam steering capabilities for the communication system and the performance increases with an increasing number of antennas. In [1] it is stated that Active Electronically Steerable Antennas (AESA) are becoming increasingly standard in modern radar systems, as the operational benefits exceed the extra complexity and costs of hardware and software. It is also concluded that the transition from GaAs to a combination of GaN/SiGe BiCMOS brings a reduction of the chip surface with a factor beyond 5:1. In [2] a 28 GHz 32-Element phased array transceiver IC is implemented in a SiGe BiCMOS process. The system consist of 32 transceivers taking 3 GHz IF inputs to 28 GHz RF output. The chip occupies an area of 165.9 mm<sup>2</sup>. In the paper it is stated that high output power comes at the cost of power consumption, cooling complexity and increased size.

Another example of a MIMO system is presented in [3] where 64- and 256-elements wafer-scale phased-array transmitters at 60 GHz in SiGe is presented. The chip consists of a mm-wave transceiver and phased array unit elements which feed on-chip dipole antennas. These blocks as well as RF distribution networks and digital control modules (in BiCMOS technology) are integrated on a single silicon chip. The area for the 64 and 256 element versions is 471 mm<sup>2</sup> and 1740 mm<sup>2</sup>

respectively. Each transmit channel has a saturated output power  $P_{Sat}$  of 3 dBm. The equivalent isotropically radiated power (EIRP) is reported to be 38 dBm for the 64 channel version. A relative drop in the EIRP of 0.5 dB was noted when all 64 channels were simultaneously driven compared to when only one channel was active. This drop was attributed to the heating of the chip as the channels were turned on. Since GaN technology enables high power at high frequency it is a strong candidate for the AESA systems. In [4], a comparison is made between GaN MMIC Ka band amplifiers relevant for 5G applications. The power levels range from 4.7 W to 8.7 W. It is reasonable to assume that integrating such amplifiers in a small area will amplify already existing heating problems in these circuits and the problems observed in [2] and [3] will be of increased concern.

It is widely known that increased temperatures degrades the performance of GaN HEMT transistors in terms of Noise Figure (NF), gain and output power. In [3], [5] it is shown how extrinsic noise performance was degraded with temperature and how access resistances (which increase with temperature) are a significant contributor to the overall noise performance of AlGaIn/GaN- HEMTs. Furthermore, in [6] it is concluded how the drain current is reduced with increased temperature, reducing both output power and gain.

It is clear from these observations that in order to predict the level of performance deterioration, there is a need to accurately determine the junction temperature of the transistor. Furthermore, it is of interest to understand how heat is transferred between the transceiver elements. This includes understanding the significance of each layer in the material structure to the heat coupling and the time constants related to each layer. Knowledge of these parameters and how they vary with distance and temperature helps to predict the impact of thermal effects and is therefore important in order to make better circuit designs.

## 1.2 Dynamic Bias Control

Traditionally an amplifier in a transmitter or receiver is designed for a specific bias supply operating point. This operating point, usually referred to as the quiescent point, will be fixed to the designed value during normal operation. The class of operation and general performance of the amplifier would then be known in a specific thermal environment and frequency band. Figure 1.1a shows a general block diagram of a Power Amplifier (PA) where the bias point does not change over time. In this case the performance of the amplifier may vary depending on the signal type and operating climate. In contrast to the setup in Figure 1.1a, a system where the bias, constantly or piecewise, does change over time is said to be a dynamic bias control system.

Figure 1.1b shows a PA where the shape of the RF frequency is tracked by the supply voltage logic which controls the type of supply voltage that feeds the amplifier. This technique is referred to as Envelope Tracking (ET) and is used to enhance the performance of the amplifier when it operates with highly amplitude modulated signals. Since the bias operating point strongly affects key parameters of the amplifier such as gain, linearity, output power and noise figure, the purpose

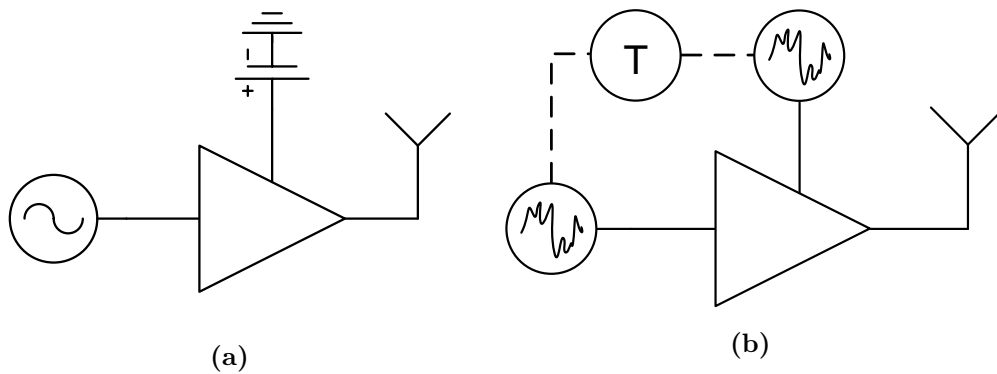


**Figure 1.1:** Example of a static bias system (a) and a dynamic bias system using envelope tracking (b).

of the control can be very different. The manner in which the amplifier is controlled is therefore strongly application and situation dependent. ET in the mobile communication industry serves to maximize efficiency and minimize nonlinear effects. Maximum efficiency is achieved close to compression, a point where nonlinear effects start to increase. An example is given in [7] where Envelope Tracking is used to maintain efficiency levels greater than 50 % in a GaN-on-SiC MMICs 12 W peak transmitter for various shapes of amplitude modulated pulses.

To ensure that parameters such as gain and power remains constant over temperature a structure shown in Figure 1.2 can be used. The structure includes a tunable attenuator at the output of the amplifier and the attenuation of the attenuator will change according to the current temperature at the amplifier. As the temperature goes up, the attenuation will go down, ensuring a constant gain over temperature. This is an example of a simple structure that handles thermal effects and is used to a limited extent in the radar industry. Although such concepts address some of the properties of dynamic bias control, a lot of possibilities are yet to be explored. Using an attenuator on the output means working around the problem of thermal heating affecting amplifiers. It solves the problem in a very inefficient way by sacrificing power to be dissipated in the attenuator, causing efficiency to drop and the temperature to increase further. What needs to be investigated and what still is

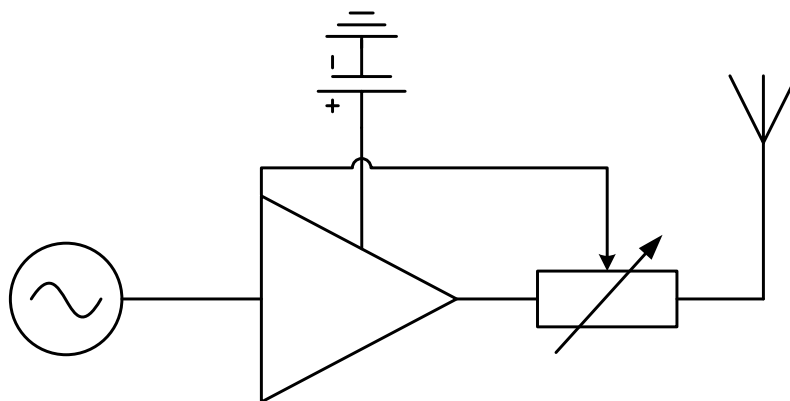


**Figure 1.2:** Temperature dependent attenuation at output.

unknown is if the thermal deterioration effects can be solved at the amplifier stage.

It is pointed out in [3] that the rise in chip temperature (and hence lower gain) was compensated by increasing the Proportional To Ambient Temperature (PTAT) current which is the current to the line amplifiers (amplifiers in each 4x4 sub-array in [3]). This concept can be applied as a general way of controlling the performance of each individual element in an array of transceivers. Figure 1.3 shows the block diagram of a dynamic bias control system in an array of transmitters. The elements are driven in a specific way that creates a desired radiation pattern. This will create a unique thermal environment for each element in the array. As a consequence the temperature for each element has to be measured separately. This information is fed back into a bias control unit which then determines the appropriate bias for each element with regard to its current thermal environment.

This bias control scheme is a possible solution to the problems in Section 1.1 and several parts of it need to be looked into. One of them is to what extent can dynamic bias control be used to prevent thermal performance deterioration in GaN transceivers. Another is how accurately it is possible to measure the junction temperature of the devices with a GaN based temperature sensor.

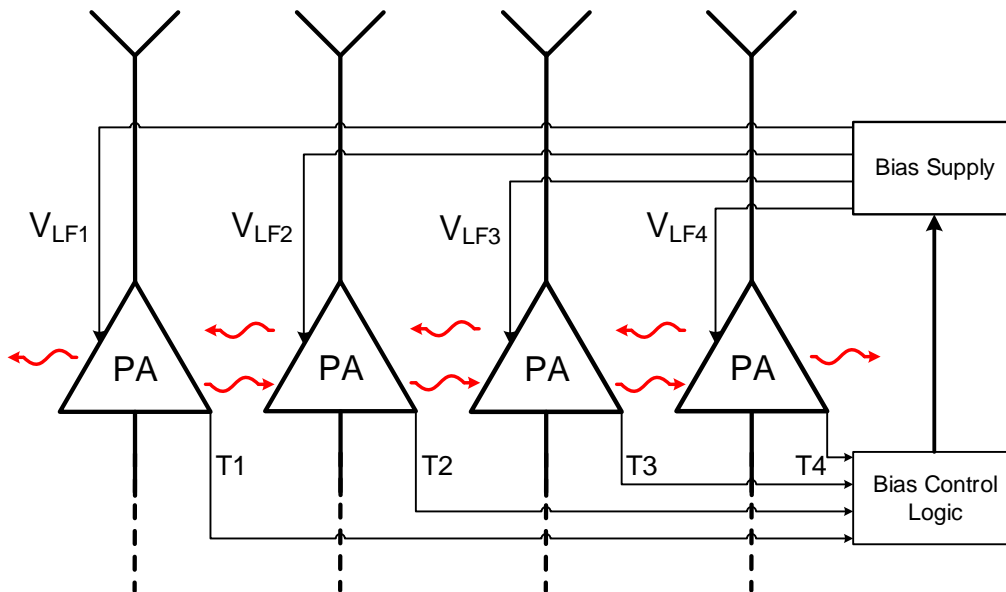


**Figure 1.3:** Array of transmitters in a MIMO system.

### 1.3 Purpose of Study and Report Structure

The purpose of this project is to study the temperature dependent performance of GaN circuits and to which extent this can be compensated for with an adaptive bias control circuit. To determine the operating temperature of each individual circuit in a multi transceiver chip, an on-wafer temperature sensor needs to be close to the circuit. The integration of this sensor, as well as a characterization of the thermal coupling across a large GaN die will be carried out to enable the bias compensation scheme to be utilized on multi transceiver chips. In chapter 2 a GaN sensor study is presented covering two process runs in Chalmers in-house GaN process [8]. The study includes two types of sensors. One mesa resistor sensor and one Schottky diode sensor. The chapter starts with the design layout of the sensors in two steps. This is followed by a description of the measurement setup for the different test structures. Next, results are presented, including IV measurements, pulsed measurements and modeling of the measurements in the following subsections. The last section covers a test of the devices to see how well the sensors work in practice.

In chapter 3 a Low Noise Amplifier (LNA) study is presented. The study covers the behaviour of the LNA versus a large bias grid with over 200 different bias points. Three LNAs manufactured in three different processes are covered. Two LNAs are designed at Saab and processed at Chalmers and UMS. The third LNA is commercially available from Qorvo<sup>1</sup>. The chapter starts with introducing key characterizing parameters for the LNAs. The studied parameters are noise figure, Output third order Intercept Point (OIP3), 1 dB compression Point (P1dB) and gain. This is followed by a description of the amplifiers under test and the measurement setup used for the LNA measurements. The results are presented, analyzed and discussed in the subsequent sections starting with the bias sweep results. This is followed by presenting the LNA performance parameters as surface plots versus the bias voltages and temperature. In the last section, a high power RF pulse measurement is presented on the Qorvo LNA. Chapter 4 summarizes the important results and conclusions of the measurements in chapter 2 & 3. Lastly, future work is suggested in chapter 5.

---

<sup>1</sup>TriQuint TGA2611, this LNA will be referred to as Qorvo in the text.





# 2

## GaN Temperature Sensor Study

As was stated in Section 1.2, knowledge of the temperature in the device is a key factor to predict the long and short term reliability and effects on performance. An integrated sensor in the used technology is the most desirable solution. In this chapter, a study on GaN based temperature sensors is performed to evaluate what type of sensor that can be used and how well the temperature can be estimated at a given distance from the heat source. The study also gives insight in the properties of propagating heatwaves in the GaN material for different distances and temperatures.

### 2.1 Sensor Design

Using the Advanced Design System (ADS) from Keysight Technologies Inc., both mesa resistors and Schottky diodes were designed to be used as temperature sensors. Several versions of these devices were designed with different dimensions (widths) at different separation distances. A first and second layout was designed, processed, and measured in the scope of the study. The results from the first design were used to significantly improve the design for the second layout area. This second area is the basis for the results presented in Section 2.3, 2.4 and 2.5.

#### 2.1.1 First Design Run

The layout area of the first run can be seen in Figure 2.1a. The structure in the area is based on two components, the heating element or "heater" and the sensor. Each row in each square in Figure 2.1a has a heater to the left and sensor to the right. The heater is a mesa resistor and the sensor to the right is either a Schottky diode or mesa resistor. The heaters were designed with different widths ranging from 25 to 50  $\mu\text{m}$  with a contact separation of 2  $\mu\text{m}$ . This resulted in current levels ranging from 20 to 50 mA at 5 V. The same mesa resistors were also used as sensors on the opposite side (Top right square in Figure 2.1a). Schottky diodes with 25  $\mu\text{m}$  gate width are used as sensors in the top left square in Figure 2.1a. The distances between the heater and sensor range from 133  $\mu\text{m}$  to 1335  $\mu\text{m}$ . A picture of the processed design is shown in Figure 2.1b.

An expanded view of the structures in the bottom left and right squares of Figure 2.1a are shown in Figure 2.2. As can be seen in the figures, these structure has a common ground metal layer in between with separation distances ranging from 10

to 50  $\mu\text{m}$ . The difference between the two types is small, in Figure 2.2a there are two mesa regions (teal boxes), with the metal in between on top of the GaN layer structure. In Figure 2.2b the two active regions have been merged into one single mesa, acting as both heater and sensor. These structures were designed to be used as test devices to test the principle of operation during pulsed measurements.

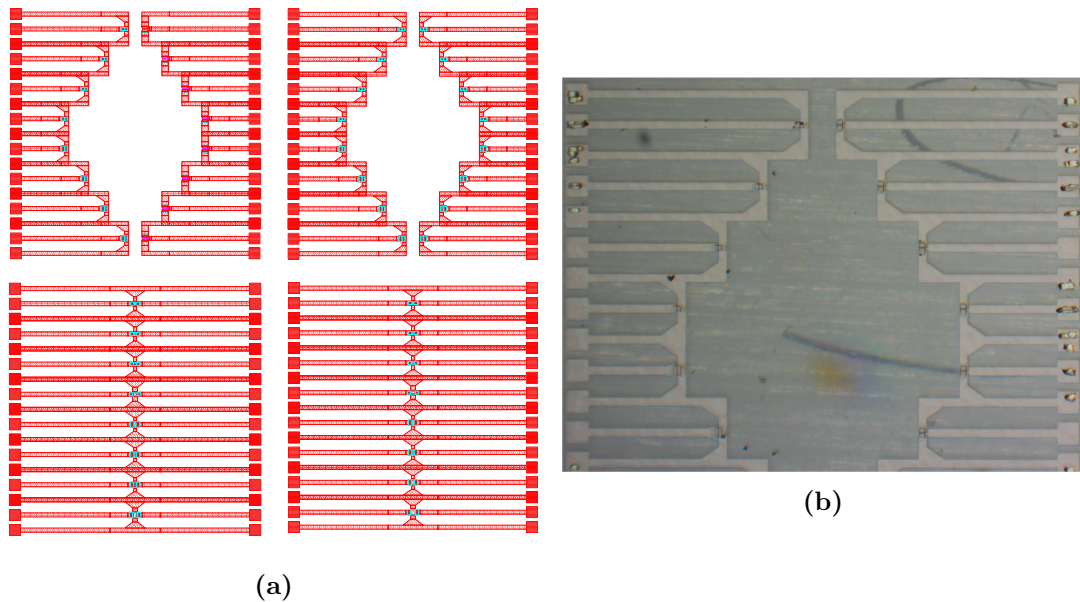


**Figure 2.1:** ADS Layout area of first design (a) and processed devices (b). Note: The black lines in the background of (b) are markings for sample identification on the backside of the transparent substrate.

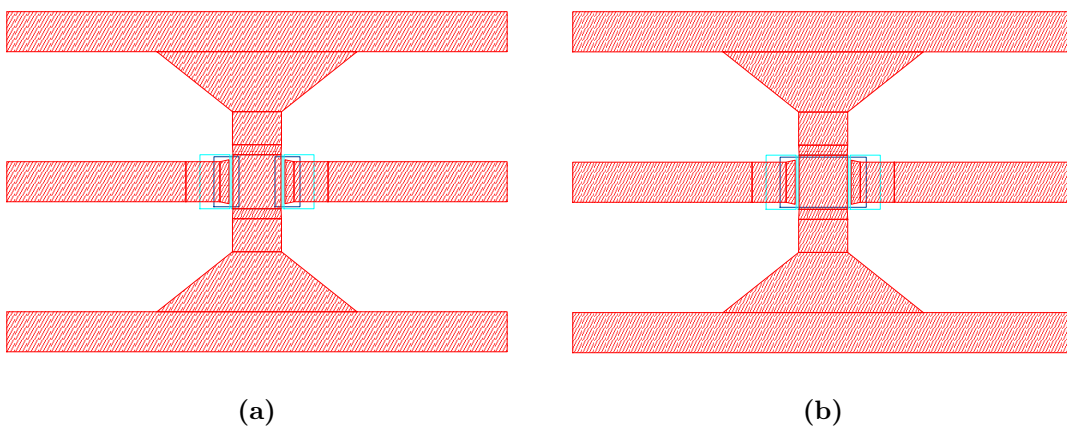


**Figure 2.2:** Principle verification structures in first layout with separate mesa (a) and common mesa (b).

## 2.1.2 Second Design Run

The second area layout is a refined version of the first layout with improvements based on the first measurement results. Figure 2.3a shows the area of the second layout in ADS. As can be seen in the figure, most squares has two columns of heaters and sensors (or sensor only). Hence the access lines have reduced length and increased width in order to decrease resistance in the lines and thus support higher power.

The area in Figure 2.3a have only mesa resistors as sensors which where designed to either  $15\ \mu\text{m}$  or  $30\ \mu\text{m}$  width. This gives lower quantization noise from the instrument by enabling a reduction in the measurement range of the sensor current (which becomes lower for smaller widths). The top right square in Figure 2.3a shows the two sensors placed at distances ranging from  $2\ \mu\text{m}$  to  $400\ \mu\text{m}$ . A similar area was also designed with a gate process included. This area uses Schottky diodes with  $25\ \mu\text{m}$  and  $50\ \mu\text{m}$  widths as sensors. These processed devices are shown in Figure 2.3b. As indicated by the figure, these diodes are placed at the same distances as the mesa sensors ( $5$  to  $400\ \mu\text{m}$  distances shown here).

The heaters in the first design provided to low power levels which were difficult for the sensors to detect. In the second design, the mesa heater resistor was increased to  $100\ \mu\text{m}$ . One  $600\ \mu\text{m}$  version was also designed consisting of six of the  $100\ \mu\text{m}$  versions in parallel. These larger heaters can be seen in the bottom and top left in Figure 2.3a. Note the larger distances available by using the sensors in the second column as sensors.

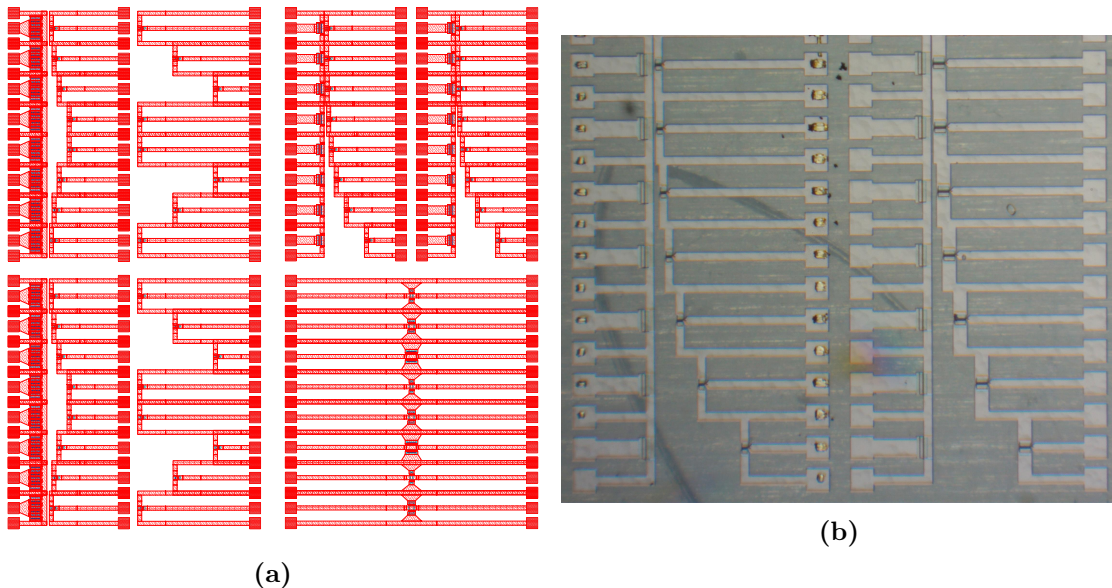


**Figure 2.3:** Design area of the second layout with mesa resistor sensors (a) and processed area with Schottky diodes (b).

An expanded view of the specific devices are shown in Figure 2.4 including the 100  $\mu\text{m}$  (2.4a) and 600  $\mu\text{m}$  (2.4b) heaters as well as the 15  $\mu\text{m}$  mesa sensor (2.4c) and 25  $\mu\text{m}$  gate width Schottky diode (2.4d). The figures include the top metal (red), ohmic contacts (teal), active regions (blue) and gate metal (pink). The final processed versions of these devices are shown in Figure 2.5 where 2.5a and 2.5b is the Schottky diode and mesa resistor placed 100  $\mu\text{m}$  from the heater respectively. These structures provide the basis for the results in the remainder of chapter 2.

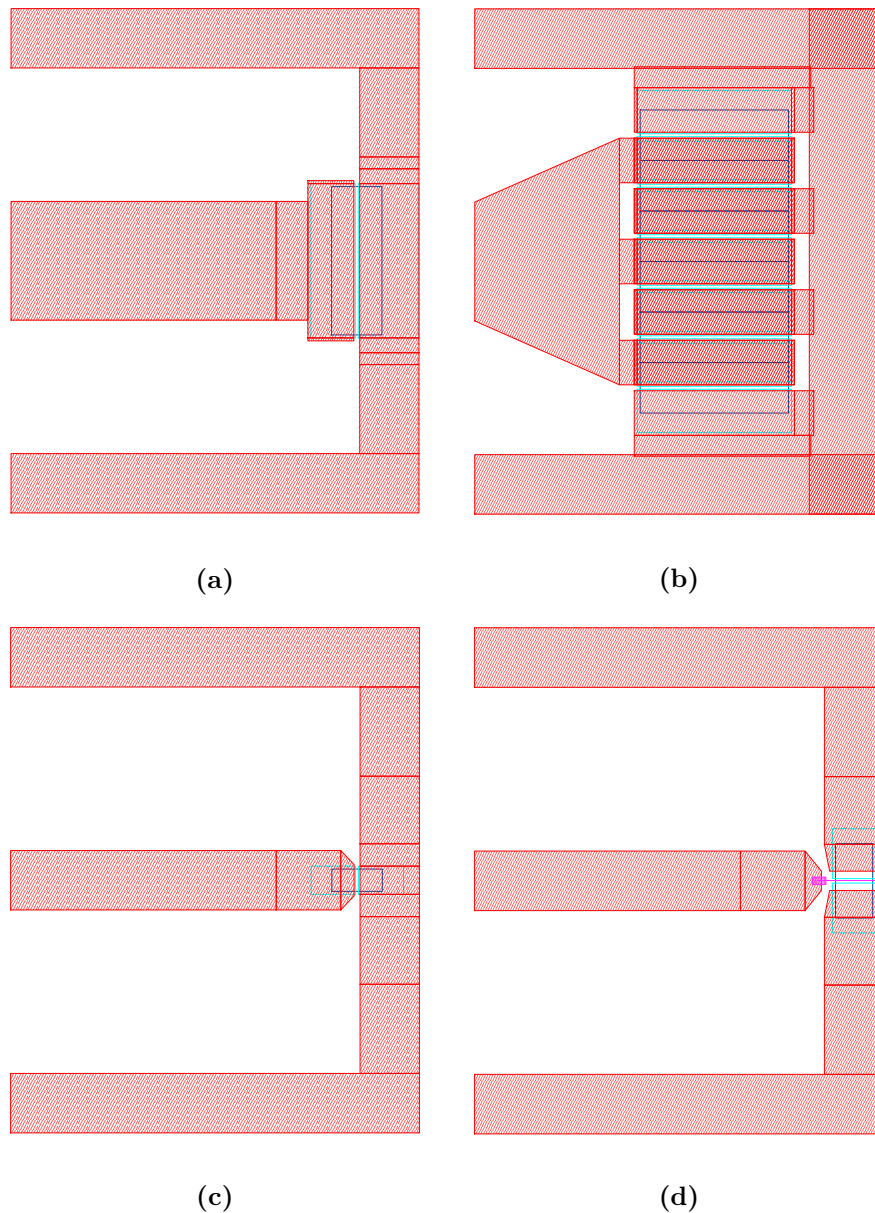
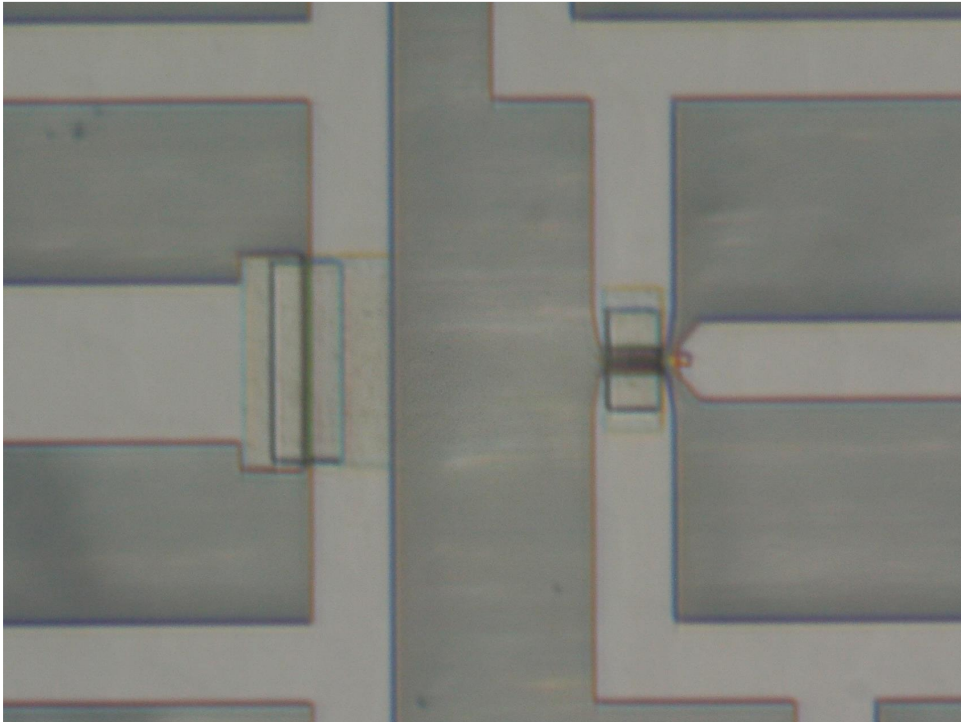
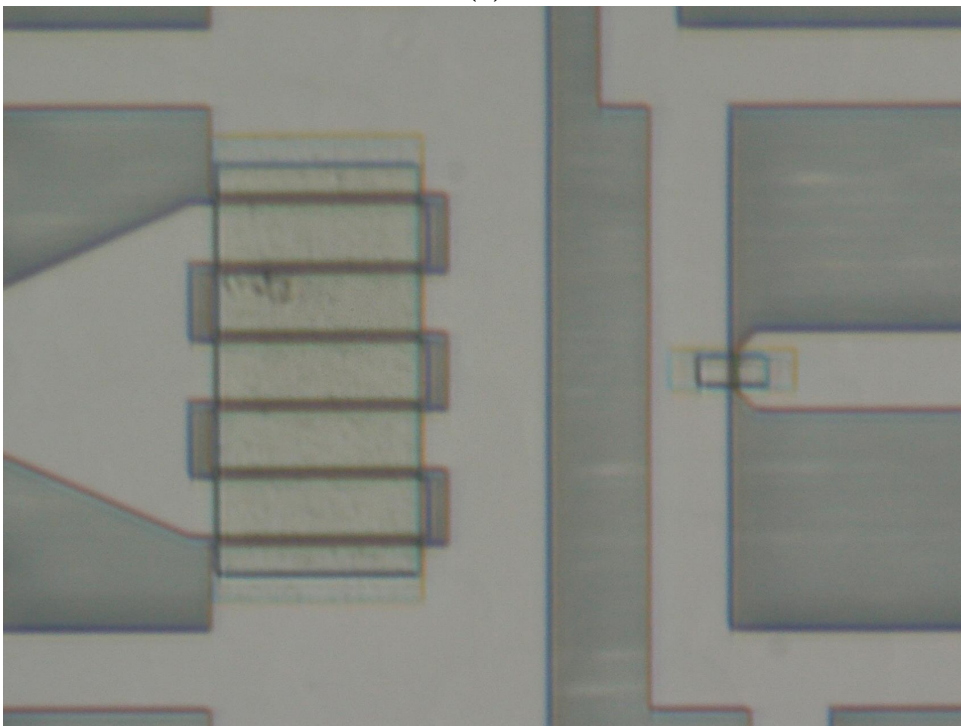


**Figure 2.4:** Sensors and heaters in the second layout. A 100  $\mu\text{m}$  heater (a) and 600  $\mu\text{m}$  heater (b). A 15  $\mu\text{m}$  mesa sensor (c) and 25  $\mu\text{m}$  Schottky sensor (d).



(a)



(b)

**Figure 2.5:** Final processed sensors and heaters with 100  $\mu\text{m}$  separation. A 100  $\mu\text{m}$  heater and 25  $\mu\text{m}$  Schottky sensor (a) and a 600  $\mu\text{m}$  heater and 15  $\mu\text{m}$  mesa sensor (b).

## 2.2 Measurement Setup

The measurement setup for the GaN sensors is built to make two key measurements. First the current versus voltage characteristics of the sensor is measured for different temperatures to pre-characterize its temperature dependence. The second measurement is to characterize the lateral thermal properties of the structure by applying a pulse to the heating element and monitor the resistance of sensors with different distances from the heater versus time. The entire measurement system used to make both these measurements is shown in Figure 2.6. Omitted in the figure is the thermal chuck which controls the backside temperature of the Device Under Test (DUT). In this case, the thermal chuck is not controlled by the computer, but set manually before each measurement starts. Furthermore, during the measurements, the DUT is placed in a probe station inside a nitrogen filled chamber with the thermal chuck as base and a plastic plastic top lid. This ensures a controlled climate in terms of temperature and humidity. The chamber, DUT and thermal chuck can be seen in Figure 2.7 where the top lid has been removed.

The setup is built around the current waveform analyzer CX3324A from Keysight Technologies which can capture current and voltage waveforms with 1 GS/s on 4 channels. The current waveforms are measured with current probes which can be connected to any channel. Similarly, voltage waveforms can be measured by connecting a voltage sense port adapter to the desired channel. In this case the CX1103A current probe is used with a sensor head for both current and voltage measurements (IV-Probe in Figure 2.6). As can be seen in the figure, channel 1,2 and 3,4 measures the current and voltage waveforms on the heater and sensor side respectively. Furthermore, the sensor is connected to a power supply that can either bias the sensor at a constant voltage (for pulsed measurements) or sweep the voltage.

The heater is connected to a high power pulser module which is supplied by a separate power supply with two channels (HP6625A). The pulser module switches between the two channels according to the input signal from the waveform generator (TG5012A). The waveform generator and current waveform analyzer are synchronized using the 10 MHz reference signal. Furthermore, the waveform generator triggers the current waveform analyzer when its signal goes high to the pulser module. All instruments are controlled by a PC that configures the instruments and acquires data via GPIB, LAN or USB interfaces.



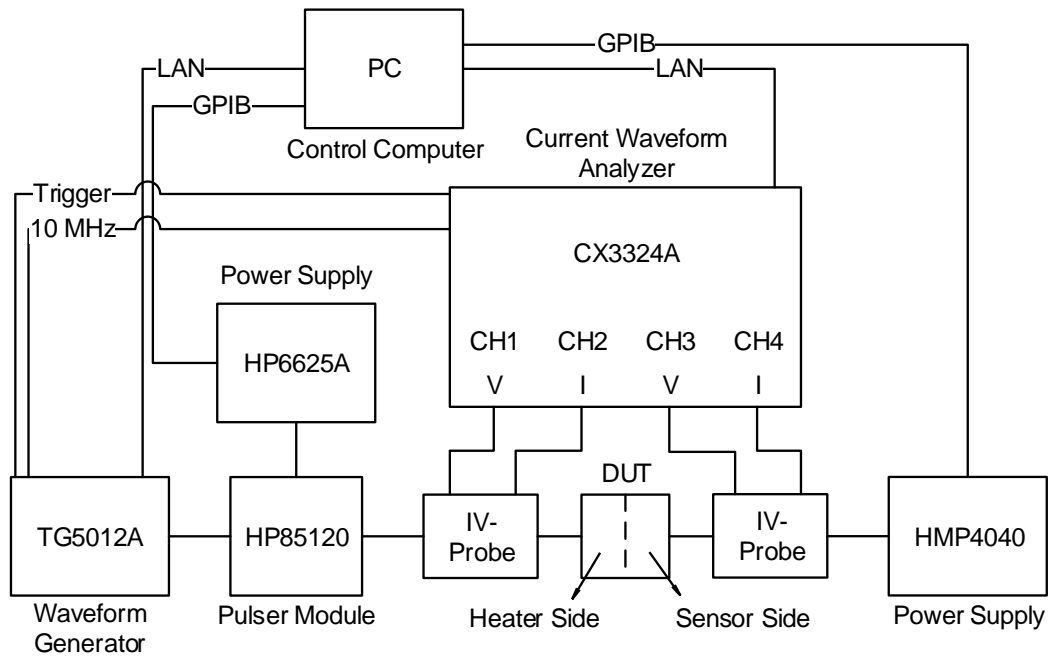


**Figure 2.6:** IV versus temperature measurement and pulse measurement setup for GaN sensors.

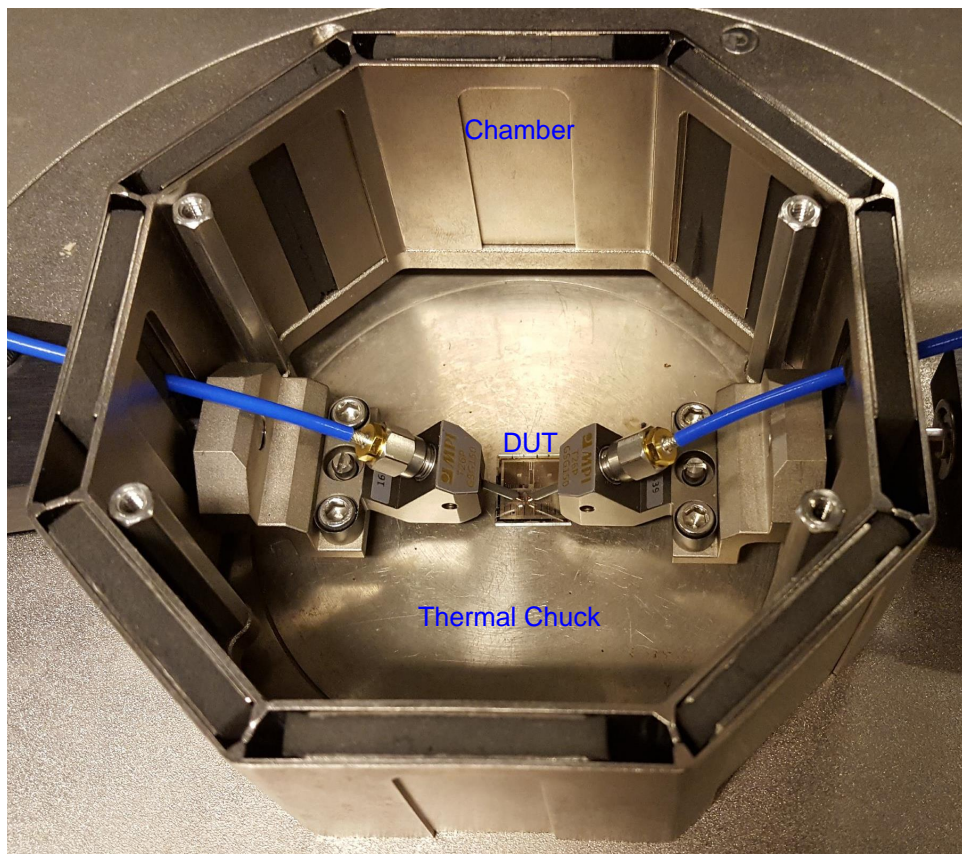


**Figure 2.7:** Climate chamber with probes and DUT inside, placed on the thermal chuck. A plastic top lid is placed on top and the chamber is filled with nitrogen during measurements.

The choice of Power Supply Unit (PSU) for pulsed measurements is important, since a constant output voltage is wanted for the sensor. Therefore, a detailed study was carried out to determine the best PSU for this purpose. The tested PSUs were the Hewlett Packard HP6625A, HAMEG HMP4040, Keithley K2400 and Hewlett Packard HP4156. Figure 2.8 demonstrates the usage of these PSUs for the sensor in Figure 2.2a. The right column shows the bias voltage applied to the sensor before and after the heater is subjected to a pulse at  $t = 0$  s. The left column shows the current response of the sensor. Apart from demonstrating the working principle of the pulsed measurements, the measurement also verifies the importance of a stable PSU. In the ideal case, the sensor voltage is unaffected by the pulse applied to the heater. However, since there is a common ground metal at the DUT in these devices, the sensor voltage is forcibly changed by the heater pulse. These voltage ripples translate to current ripples and therefore contaminates the actual current response measurement. Clearly the HMP4040 power supply has the most stable voltage level before and after the pulse. It is most likely due to the fact that the PSU does not detect the ground disturbance and therefore does not start to compensate for it which is the case for the other PSUs.

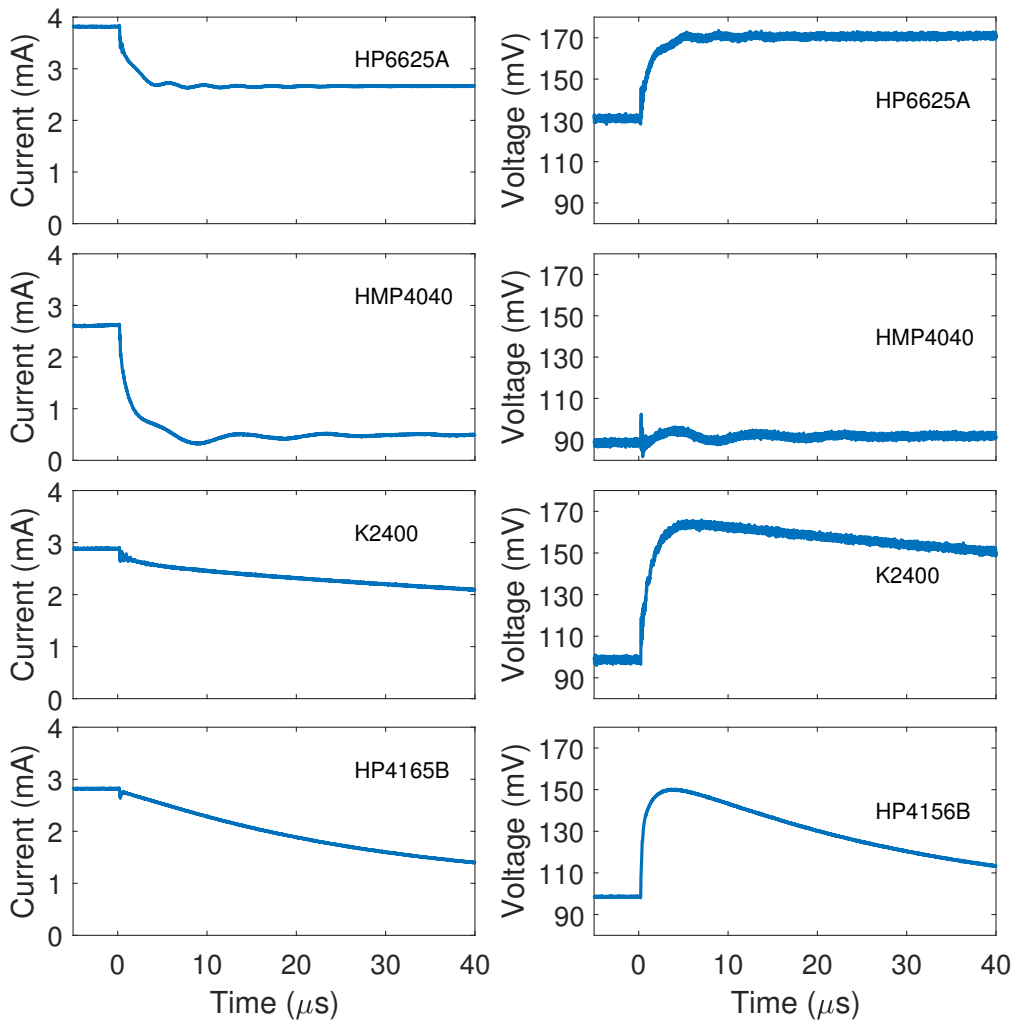


Figure 2.8: Comparison of PSU impact on measurement.



## 2.3 IV Measurements

The IV versus temperature (T) measurements provides a good characterization of the device and gives insight about the temperature dependence and whereabouts of key parameters such as the threshold voltage  $V_T$  for the Schottky diode and saturation current level for the mesa resistors.

### 2.3.1 First Design Run

A typical IV versus T measurement for the first run is shown in Figure 2.9a for the 50  $\mu\text{m}$  mesa resistor and in Figure 2.9b for the 25  $\mu\text{m}$  Schottky diode. Several versions of the mesa resistors were designed in Section 2.9a and the difference in the IV measurements is mainly a scaling of the current magnitude if the width is increased/decreased. As seen in Figure 2.9a, a voltage sweep from -5 to 5 V results in a linear region from approximately -1 V to 1 V, and a saturation region outside this range. In the linear region, a decreasing conductance  $\sigma$  with increasing temperature is observed. This is expected since the electron mobility decreases as the temperature increases [6]. In the saturation region however, there is a change in sign of  $d\sigma/dT$  and the conductivity increases as the temperature increases. A possible explanation is that the higher electric field increases the rate of electron trapping which in turn decreases the amount of charge carriers in the channel. As the temperature then increases, the release rate of the electrons is increased, resulting in more charge carriers as the temperature increases [9].

The IV versus T measurement for the Schottky diode is shown in Figure 2.9b. In this case the voltage sweep ranges from 0.1 V to -15 V to make a reverse bias IV characterization versus T. It can be seen that the diode has a larger current derivative with respect to T close to the avalanche breakdown voltage. The diodes proved to have a significant spread between different individuals in terms of breakdown voltage level.

The first devices proved to have a number of drawbacks. Using a 50  $\mu\text{m}$  mesa as sensor resulted in difficulties measuring the response properly for the pulsed measurements. When the sensor is biased at around 1 V it gives a starting current above 20 mA which is the upper limit for one of the lower current range modes for the current waveform analyzer. The response during the pulse is in the order of  $\mu\text{A}$  and therefore drowns in the quantization noise. Furthermore, using the 50  $\mu\text{m}$  mesa as heater resulted in very low dissipated power levels ( $<1.2\text{ W}$ ), which further complicated the detection. It is also possible that significant power was dissipated in the access lines. These lines were proven too thin and started to fuse when the voltage reached levels around 25 V. The heater current was not measured for the first run but can in this case be assumed to be greater than 50 mA. Testing the maximum currents (or voltage levels in this case) also indicated the need for redundancy copies in the layout. Finally, the shortest separation distance proved to be too large to properly study the distance dependence and its impact on the response.

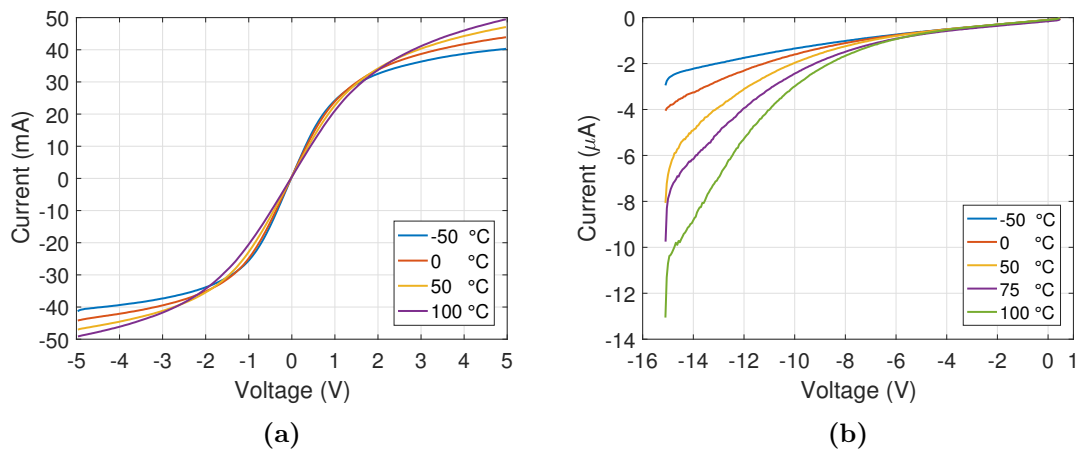


**Figure 2.9:** First layout IV versus T characteristics of a 50  $\mu\text{m}$  mesa resistor (a) and 25  $\mu\text{m}$  Schottky diode (b)

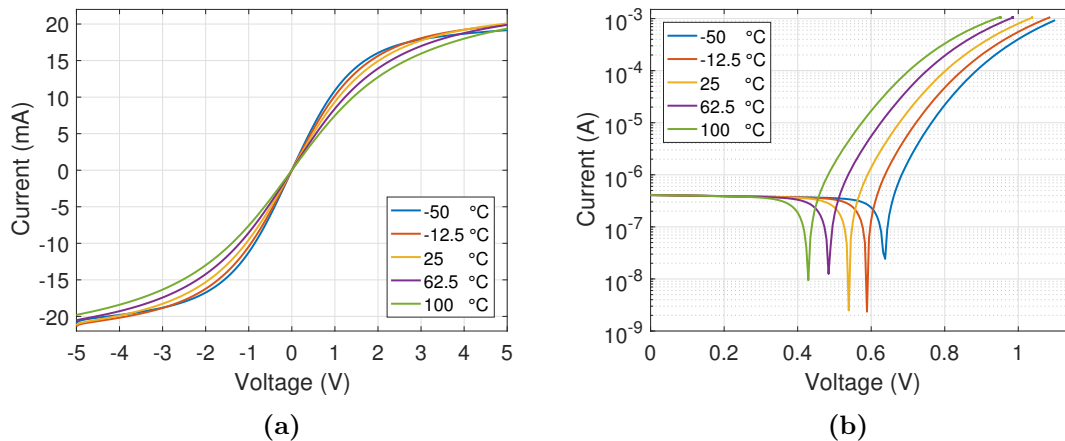


**Figure 2.10:** Second layout IV versus T characteristics of a 15  $\mu\text{m}$  mesa resistor (a) and 25  $\mu\text{m}$  Schottky diode (b)

### 2.3.2 Second Design Run

The second layout IV measurement for a 15  $\mu\text{m}$  mesa resistor is shown in Figure 2.10a. The measurement settings are the same as for the first run and the result shows two major differences. The change in sign of the conductance is more or less absent and the resistor has an expected behaviour versus temperature, with increasing resistance up to 5 V. The resistor is less than one third of the width but has almost half the current compared to the 50  $\mu\text{m}$  version in the first run in the saturation region. These differences shows the sensitivity of e.g. ohmic contact resistance which may differ between runs.

Because of the difficulties with the large variation in the reverse biased IV characteristics of the Schottky diode in the first run, the sweep range was changed to measure the diode forward biased. The IV versus T characteristics of the forward

biased Schottky diode can be seen in Figure 2.10b. It can be seen that  $V_T$  is shifted towards 0 V as the temperature increases and the current increases by more than 1000 times over approximately 600 mV in the conduction region. The plot shows the magnitude of the current. Hence the current in the off region should be negative.

## 2.4 Pulsed Measurements

In this section, the heater is subjected to high power pulses which will be dissipated in the resistor and produce heatwaves that will propagate in all 3 dimensions from the heater into the GaN hetero structure. The results from Section 2.3.2 will be used to bias the sensors in its most temperature sensitive area. In the case of the mesa resistor, the area of interest is the area close to the end of the linear region partly because the devices exhibit the strongest dependence there and partly because biasing in the saturation region only serves to increase the self heating effects. These effects are due to the biasing power consumption and can cause severe measurement errors. After selecting an appropriate bias, the sensor current is then monitored during the measurement in order to detect any temperature changes caused by the propagating heatwaves.

The sensor response will be analyzed and modeled and parameters such as time constants and delay of the current response are then extracted. Furthermore, the  $I(T)$  dependence will be modelled and the expressions are used to determine the measured temperature of the sensors.

### 2.4.1 Distance Dependence

The mesa IV measurement in Figure 2.10a indicates a good temperature sensitivity at 1.3 V. Using this bias point, and an input pulse amplitude of 20 V gives the response shown in Figure 2.11a. In the figure, the pulse on time  $t_{on}$  is 4.75 ms, the dissipated power in the heater is about 3 W, the distance to the sensor is 2  $\mu\text{m}$  and the thermal chuck temperature is 25  $^\circ\text{C}$ . The sensor current is clearly affected by the pulse and decreases as the temperature increases. After the pulse has ended, the current recovers in a reverse manner. In order to make sure a full recovery the pulse period  $T_p$  is set to 200 ms giving a duty cycle  $D = 4.75/200 = 2.38 \%$ . Finally, the sampling frequency  $f_s$  is set to 10 MS/s which is a good compromise between capturing fast transients and suppressing high frequency noise. The light in the test environment proved to have significant influence on the measurement. Figure 2.12a shows the same measurement as in Figure 2.11a in a dark and light environment. It can be seen that the current decreases in a dark environment. The current reduction continues as more time passes and even though the changes become smaller, the blue curve gets shifting downwards. Figure 2.12b shows how the IV versus T measurement for the Schottky diode is affected by the light. The sweeps for 100  $^\circ\text{C}$  and 62.5  $^\circ\text{C}$  were measured at another occasion than the other three temperatures. This caused a gap to occur in the characteristics which introduces

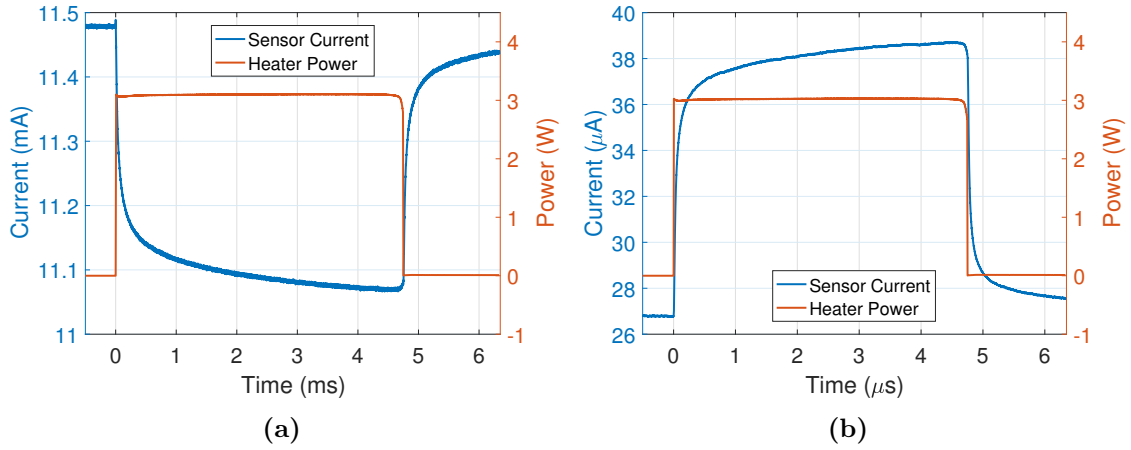


**Figure 2.11:** Pulsed measurement with 2  $\mu\text{m}$  separation distance with a 15  $\mu\text{m}$  mesa sensor (a) and a 25  $\mu\text{m}$  Schottky diode (b).

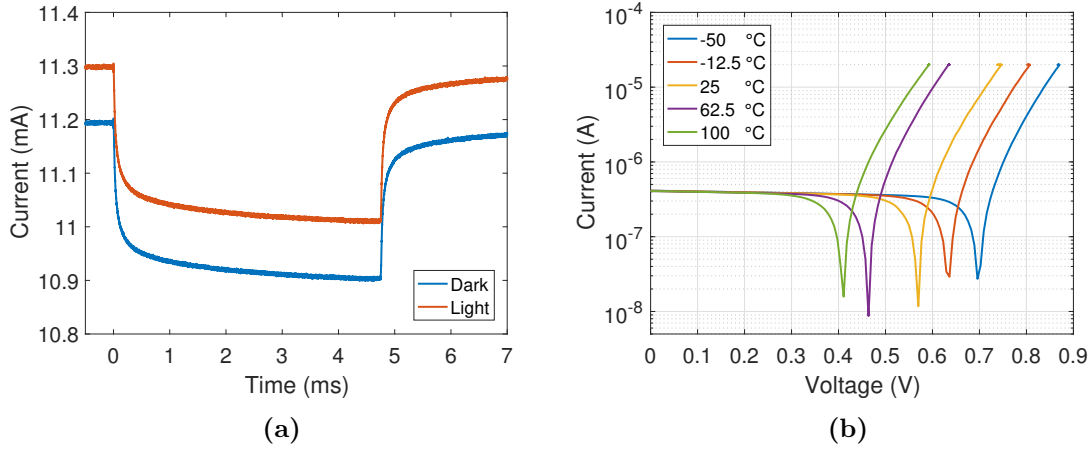


**Figure 2.12:** Pulsed measurement in a dark and light environment (a) and current drift caused by light in an IV versus T measurement (b).

errors in the biasing and temperature estimation of the diode. A possible explanation for the light dependency is the interaction of photons with trapped electrons. By illuminating the hetero structure with photons, the rate of traps released is increased and thus the current is increased. The measurements in the following sections were performed after approximately 2 min of darkness had passed.

With the bias and measurement settings kept constant as described above, the 15  $\mu\text{m}$  mesa sensor current response can be evaluated versus the distances seen in Figure 2.3. The distances are 2, 5, 10, 25, 50, 100 and 200  $\mu\text{m}$ . Figure 2.13a shows the response from each sensor at the given distance. The figure shows a spread in the quiescent current for each device which is due to the spread in resistance between individuals. The response is different in magnitude and shape at different distances and approximately reaches a steady state during the  $t_{on}$  time at the shorter distances (2-10  $\mu\text{m}$ ). Figure 2.13b shows the same figure but with the starting offset level (quiescent current) subtracted for each curve. This figure clearly shows how the magnitude of the current response decreases with distance. The derivative

$dI/dT|_{T=25^\circ\text{C}}$  is assumed to have small differences between each copy. This explains why the response of the 2  $\mu\text{m}$  sensor is slightly smaller compared to the sensor at 5  $\mu\text{m}$ . A fast transient change occurs in the order of  $\mu\text{s}$  and it becomes less apparent as the distance increases.

The different sequences and propagation delay can be seen by plotting the response versus a logarithmic time as shown in Figure 2.14. The figure shows that the delay ranges from roughly 10  $\mu\text{s}$  to 100  $\mu\text{s}$  between the longest and shortest distances. It is also visible how the fast sequence occurs within 100  $\mu\text{s}$  for the shorter distances.

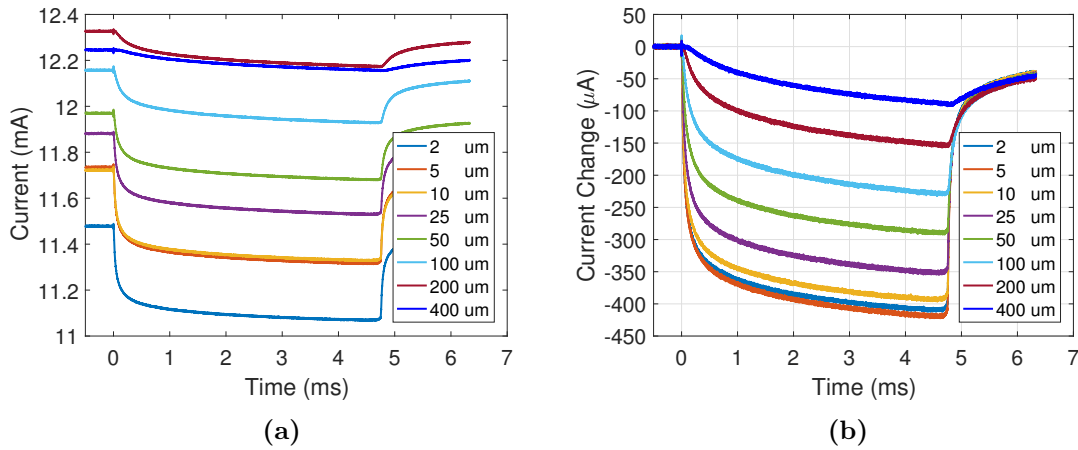


**Figure 2.13:** Current response of the 15  $\mu\text{m}$  mesa sensor biased at  $V_b = 1.301\text{ V}$  at  $25^\circ\text{C}$  with start offsets (a) and with start offsets subtracted (b).

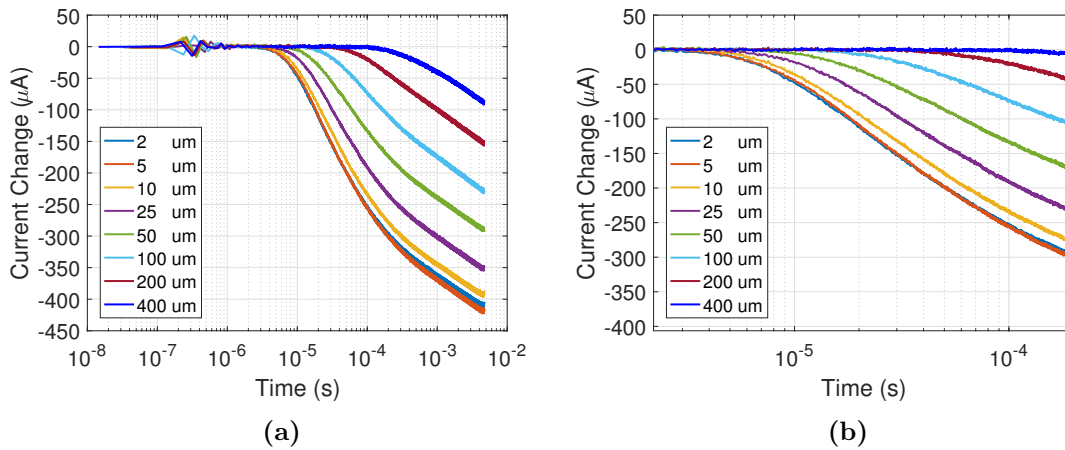


**Figure 2.14:** Current response with logarithmic x axis scale and subtracted offset with full view (a) and zoomed view (b).

The same pulsed measurement was also performed on the 25  $\mu\text{m}$  Schottky diode. During the initial measurements of the first design run. It was discovered that a reverse biased Schottky diode had very unpredictable temperature dependence and a very small response. This introduced significant amounts of quantization noise from the instrument whose ranges did not fit well to the response. For the measurements

of the second run, the Schottky diode was instead forward biased in the vicinity of the threshold voltage  $V_T$ . Between the different individuals,  $V_T$  proved to have a spread in the order of mV. The spread has a large impact on the current response (see IV plot). Hence  $V_b$  for one individual could be inappropriate for the diode at the next distance. This required a tuned bias voltage to be selected from the IV versus T characteristics for each device. For this reason, only the first four distances were measured with this sensor. Figure 2.11b presents a pulsed measurement for the Schottky diode. The diode is biased at 0.704 V which is a good point for the 2  $\mu\text{m}$  separation as seen in the IV characteristics in Figure 2.10. The responses for the first 4 distances can be seen in Figure 2.15a-b. The responses are similar to those of the mesa sensors but with an opposite sign in the change. The derivative  $dI/dT|_{T=25^\circ\text{C}}$  is very sensitive to changes in  $V_b$  or  $V_T$ . This is evident from Figure 2.15b which indicates a higher response from the sensor at 25  $\mu\text{m}$  compared to 10  $\mu\text{m}$ , meaning that the sensor at 25  $\mu\text{m}$  has a different  $V_T$  and therefore a different (higher)  $dI/dT|_{T=25^\circ\text{C}}$ .

The logarithmic plots in Figure 2.15c and 2.15d indicate a similar delay as for the mesa sensors. The slope of the response at about 1 ms also indicate the presence of similar time constants as with the mesa sensor.

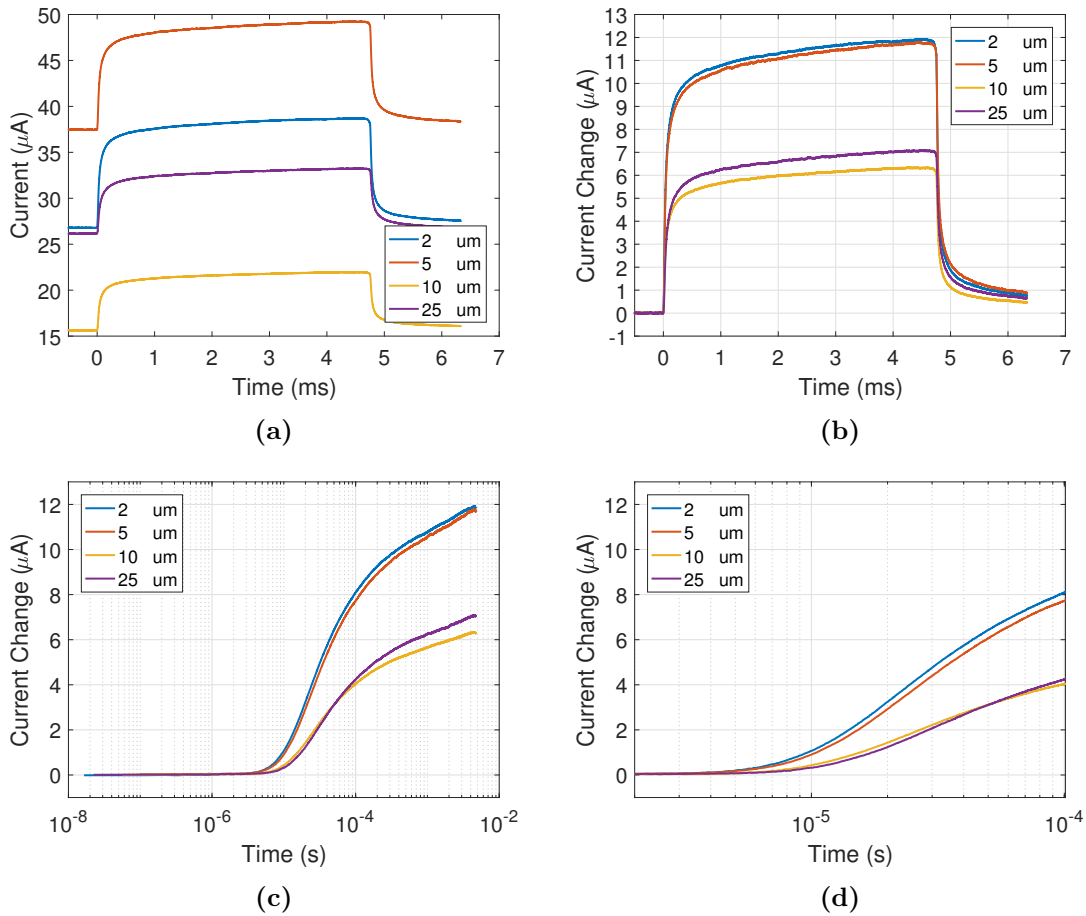


**Figure 2.15:** Current response of the 25  $\mu\text{m}$  Schottky diode biased at  $V_b = 0.704$  V at  $25^\circ\text{C}$  with startlevels (a) and with start offset subtracted (b). Current response with logarithmic x axis scale and subtracted offset with full view (c) and zoomed view (d).

## 2.4.2 Temperature Dependence

In this section, the sensors are evaluated at different measurement temperatures with the distance between the heater and sensor kept fixed. The measurement temperatures are -50, 25 and 100 °C.

From the IV measurements, the current dependence for the mesa sensor biased at the end of the linear region predicts an increased current for lower temperatures. This can also be seen in Figure 2.16a which shows the pulsed measurement performed at the three temperatures. The offset start level is higher for lower temperatures but the response magnitude is smaller and vice versa. The different sequences (time constants) are also present for all three cases but is less visible for the lower temperature because of the smaller magnitude in the response. It can be more easily seen in Figure 2.17b where the axes are logarithmic. In the figure, the shape of the responses can be seen to be very similar apart from the magnitude and delay.

It can be seen from Figure 2.16b that going from a measurement temperature of 100 °C to -50 °C results in a decreased response magnitude of roughly 350  $\mu\text{A}$ . At the same time the sensitivity is very constant as will be seen in Section 2.5.2. It is therefore concluded that the measured temperature change is much lower when the measurement is made at -50 °C compared to 100 °C even though the heater power is the same for both cases.

For the Schottky diode the trend is the opposite for the start level compared to the mesa sensor. Figure 2.18a shows the response of the sensor at the three temperatures. The offset start for the current level is higher at 100 °C as expected from the IV characteristics in Figure 2.10b, and decreases with decreasing temperature. The magnitude of the response in Figure 2.18b is strongly decreasing with decreasing temperature. This indicates that the derivative of the  $I(T)$  characteristics is a varying function of temperature for the Schottky diode. This is also verified in Section 2.5.2.

Logarithmic plots are shown in Figure 2.19a and 2.19b. In the latter, it is clear that even though the response is small at -50 °C the different sequences are still present.

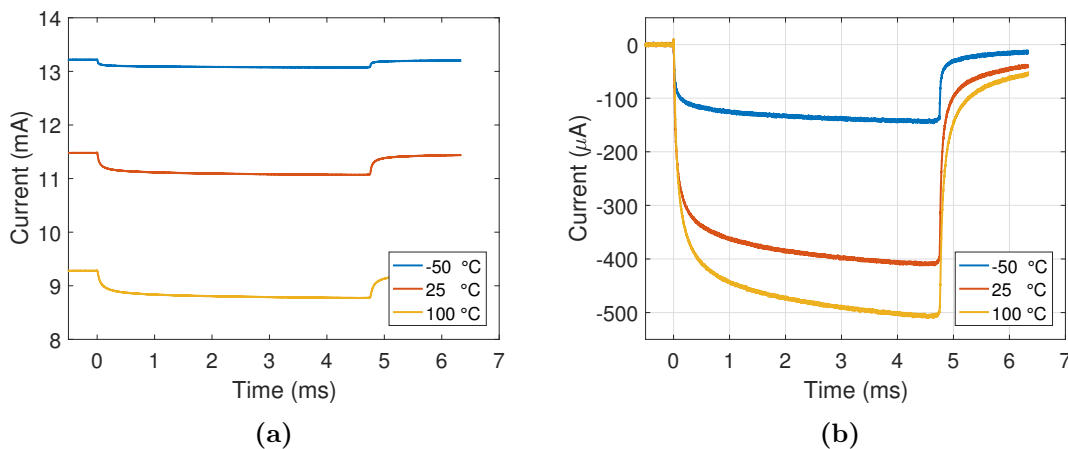


**Figure 2.16:** Current response of the 15  $\mu\text{m}$  mesa sensor biased at  $V_b = 1.301$  V at -50, 25 and 100 °C with start offset (a) and with start offset subtracted (b).

## 2. GaN Temperature Sensor Study

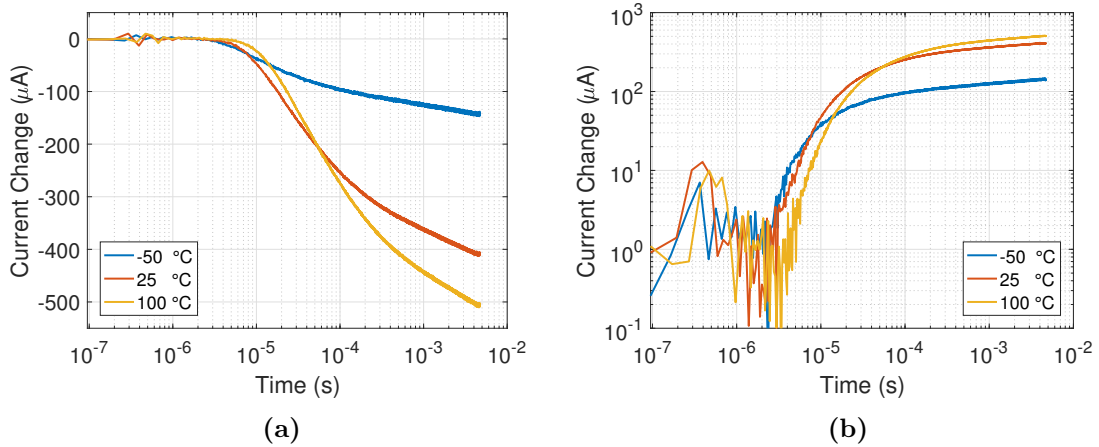


**Figure 2.17:** Current response of the 15 μm mesa sensor biased at  $V_b = 1.301$  V at -50, 25 and 100 °C with logarithmic x axis (a) and both axes logarithmic (b).

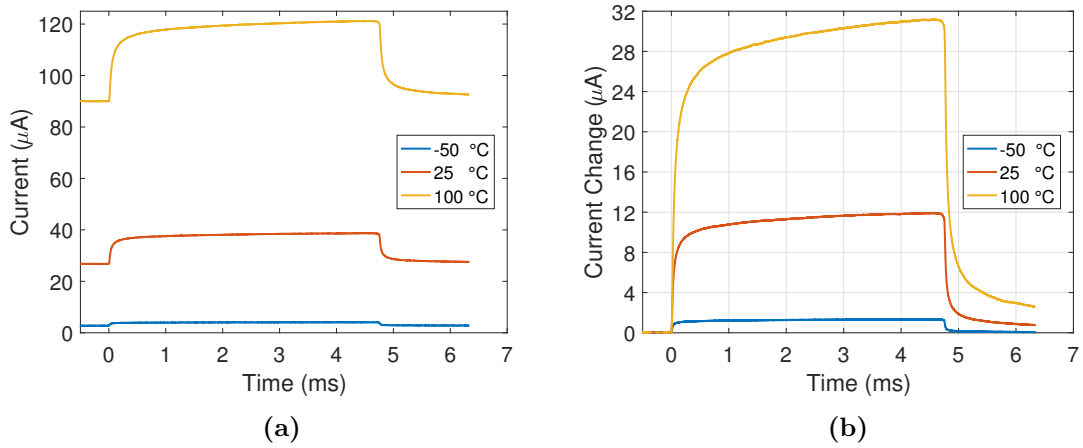


**Figure 2.18:** Current response of the 25 μm Schottky diode sensor biased at  $V_b = 0.704$  V at -50, 25 and 100 °C with start offset (a) and with start offset subtracted (b).

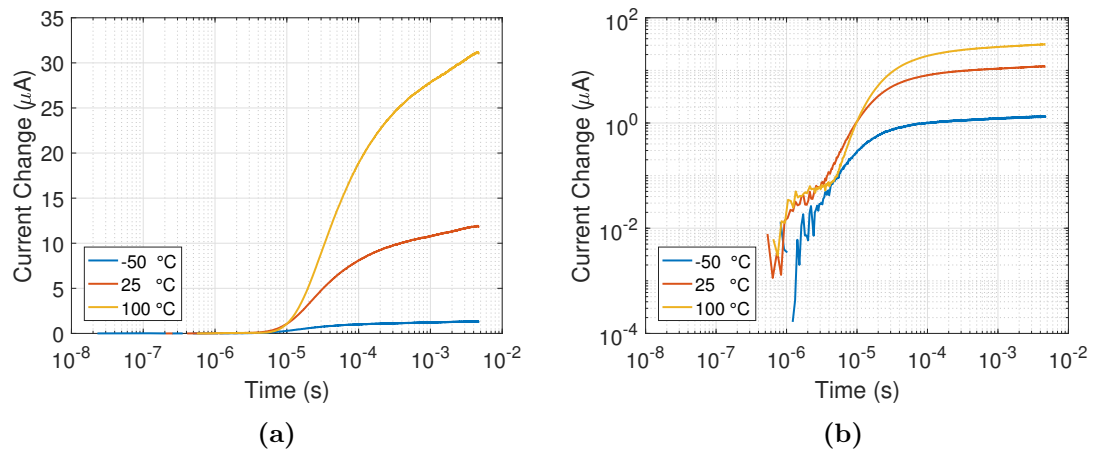


**Figure 2.19:** Current response of the 25 μm Schottky diode sensor biased at  $V_b = 0.704$  V at -50, 25 and 100 °C with logarithmic x axis (a) and both axes logarithmic (b).



## 2.5 Modeling

In this section, the results from the pulsed measurements in Section 2.4 and the IV versus T measurements in Section 2.3 are analyzed and modelled. The analytic expressions of the pulsed measurements provide more accurate information about the propagation delay, heat coupling paths and material properties of the GaN on SiC structure. The modelling of the  $I(T)$  dependence gives more insight into the temperature sensitivity and measured values of the sensors.

### 2.5.1 Current Response

The current responses of the mesa sensors in Figure 2.14 have a number of regions where the slope remains constant until it enters another region. These different sequences of the response is believed to be contributions from different thermal coupling paths to the sensor. A model of the main heat coupling paths is presented in Figure 2.20. The figure shows the heater to the left and sensor to the right with the different layers in the structure. The main coupling is assumed to occur in the GaN and SiC layers as well as a smaller coupling through the bottom of the device (thermal chuck). The different sequences following from these coupling paths can mathematically be modelled by exponential terms with time constants and amplitude coefficients. One exponential term to each path in Figure 2.20 gives three terms for this simple model. The time constants and amplitude coefficients indicate how fast the sequence of the specific path is and the magnitude of the heatwave related to that path. Furthermore, a delay  $t - t_{delay}$  has to be introduced where  $t_{delay}$  is the time it takes for the fastest heatwave to reach the sensor. Hence the function should have a constant value and start the sequence at  $t = t_{delay}$ . The following expression can be used to model the current response versus distance for the 15  $\mu\text{m}$  mesa sensor.

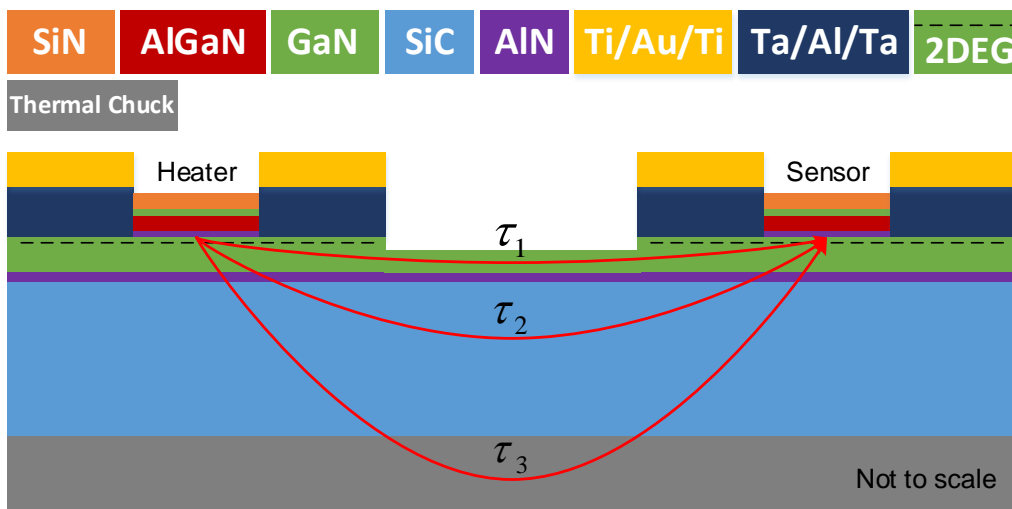


Figure 2.20: Simple heat transfer model in the GaN on SiC structure.

$$I_m(t) = I_0 + \sigma(t - t_{delay}) \sum_{n=1}^3 A_n (e^{-(t-t_{delay})/\tau_n} - 1) \quad (2.1)$$

where

$$\sigma(t - t_{delay}) = \begin{cases} 0, & t - t_{delay} < 1 \\ 1 & t - t_{delay} \geq 1 \end{cases} \quad (2.2)$$

From this expression, the propagation delay is directly given by  $t_{delay}$  and three time constants are given from  $\tau_1$ ,  $\tau_2$  and  $\tau_3$ . As seen from (2.1) and (2.2) the function remains at the start offset when  $t < t_{delay}$  (before the heatwave reaches the sensor and the response sequence starts). Figure 2.21 shows the measured current response at 25 °C of the mesa sensor together with the response based on the model in (2.1). The optimum fit was obtained using the Least Squares nonlinear function in MATLAB. The figure shows a good fit between the measured data and proposed model.

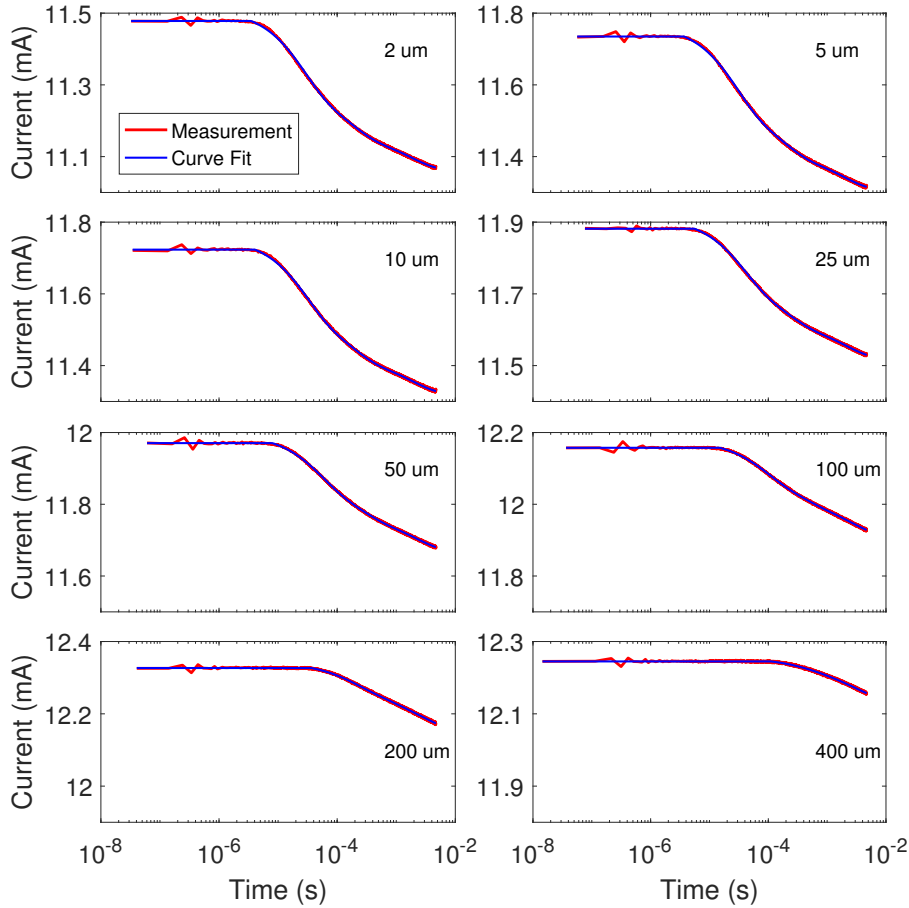


**Figure 2.21:** Measurement data of the current response of the 15  $\mu\text{m}$  mesa sensor at 25 °C and fitted response from model for separation distances 2-400  $\mu\text{m}$ .

The propagation delay is plotted versus distance in Figure 2.22e and ranges from a few  $\mu\text{s}$  for 2-10  $\mu\text{m}$  to 100  $\mu\text{s}$  for 400  $\mu\text{m}$ . The time constants  $\tau_{1,2,3}$  are plotted versus distance in Figure 2.22a. Lastly, the associated amplitude coefficients for the fit at 25 °C are plotted in Figure 2.22b.

The time constant  $\tau_1$  is most likely the heat transfer in the GaN layer between the sensor and heater. This assumption is supported by Figure 2.22a and 2.22b which shows that the fast time constant  $\tau_1$  also has the largest amplitude coefficient for the shorter distances meaning it contributes with the largest impact on the sensor response. This is expected since in that case, the path in the GaN layer is the shortest path for the heat to be transferred and the path where the attenuation of the waves will be minimized, resulting in higher values of  $A_1$ .

With the exception of a thin layer of aluminum Nitride (AlN), the next layer after the GaN layer is the Silicon Carbide (SiC) base. This is the thickest layer in the structure and is about 500  $\mu\text{m}$ . A possible interpretation of the time constant  $\tau_2$  is the heat transfer in this layer. It can be seen in Figure 2.22b and 2.22a to have the second largest amplitude coefficient for the shorter distances as well as longer time constants. As the distance increases, the amplitude coefficient  $A_1$  seems to decrease faster than  $A_2$ . This implies that the thermal resistance is higher for the GaN layer compared to the SiC layer. Therefore, as the distance increases, the influence of the lower thermal resistance in the SiC layer becomes larger and reaches a point where it exceeds the GaN layer as the primary heat transfer path between the heater and sensor.

In general,  $\tau_1$  and  $\tau_2$  both increase with distance. Figure 2.22c also indicates that this behaviour seems to be nonlinear with respect to temperature (at longer distances). The behaviour of  $\tau_3$  and  $A_3$  is divergent compared to the other two terms in (2.1). This slow time constant is believed to be an additional heat contribution through the thermal chuck. Since it involves a direct connection with the thermal chuck, it is possible that this path is affected by (mixed with) the heat source from the thermal chuck itself, explaining why  $A_3$  shows almost no dependence on the distance.

Figure 2.22c, 2.22d and 2.22e shows the temperature dependence of  $\tau_1$ ,  $A_1$  and propagation delay respectively. It can be observed that the response time in the GaN layer increases with increased temperature. Furthermore, the associated  $A_1$  coefficient also decreases with decreasing temperature which is in accordance with Figure 2.16b which showed a decreased magnitude of the response with decreasing temperatures.

Figure 2.22f shows  $A_1$  normalized to the sum of the coefficients  $A_1, A_2, A_3$ . It can be observed that for the shorter distances the influence of  $A_1$  seems to decrease faster than those of  $A_2, A_3$  as the temperature increases. Finally, the propagation delay is shown in Figure 2.22e and can be seen to increase with temperature, indicating decreased propagation velocities at higher temperatures.

The behaviour of  $A_1$  in Figure 2.22d shows that the amplitude of the fast lateral coupling is decreasing from roughly 225  $\mu\text{A}$  at 100 °C to 75  $\mu\text{A}$  at -50 °C for the 2  $\mu\text{m}$  distance. This clearly indicates a reduced temperature at the sensor. It is believed that the heat from the pulse is conducted into other directions before reaching the sensor. Consequently, a lower temperature is measured.

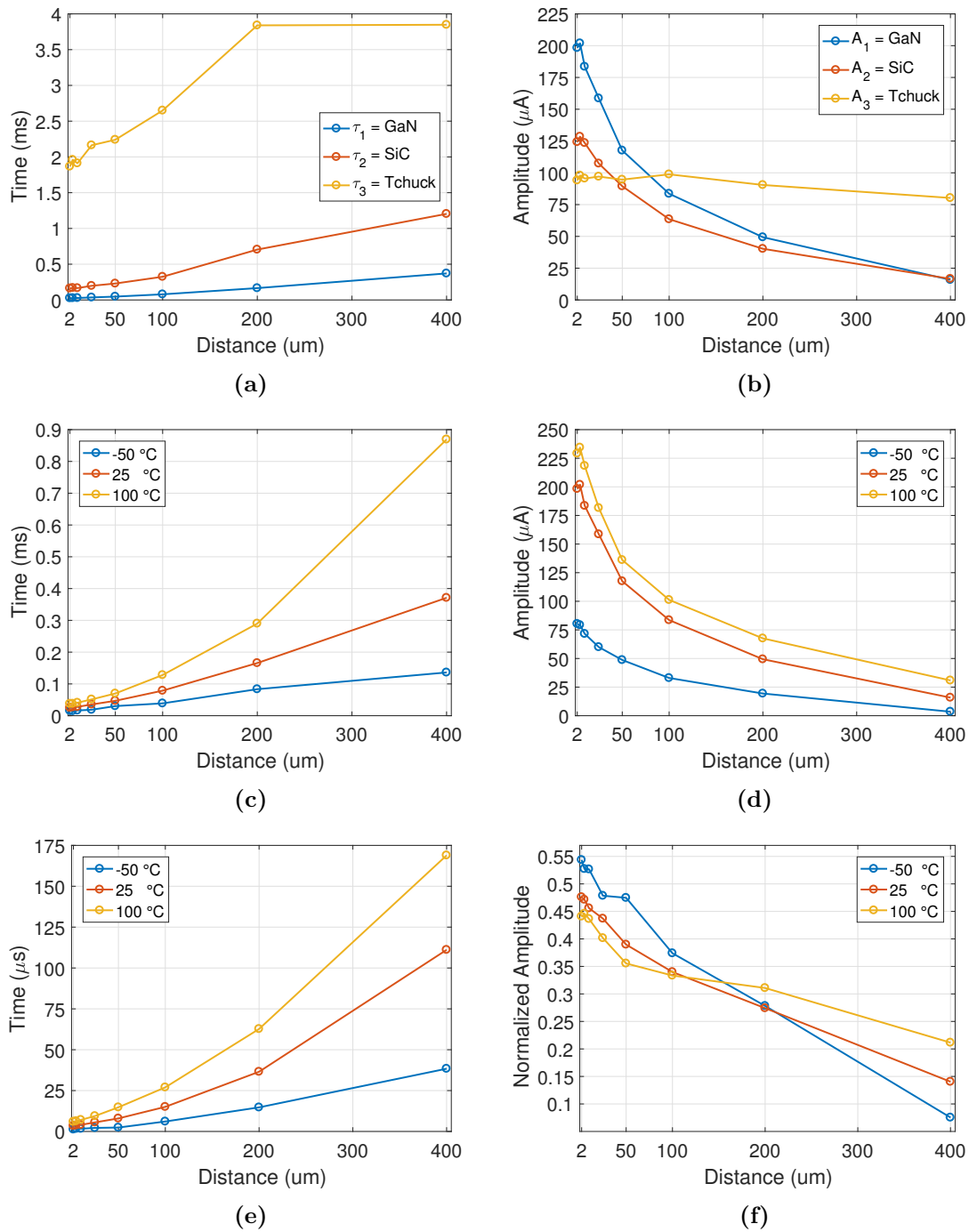


**Figure 2.22:** Time constants of the exponential terms for extracted model at 25 °C (a) and corresponding amplitude coefficients (b) as well as temperature dependence of fast lateral coupling in the GaN layer (c). Temperature dependence of GaN amplitude coefficient  $A_1$  (d) normalized to total sum of coefficients  $A_{1-3}$  (f). Lastly, (e) shows the temperature dependence on the propagation delay.

## 2.5.2 IV Characteristics

The next step in the model analysis is to extract models from the IV characterization in Section 2.3. It is proposed in [10] that the mesa resistors can be modeled with the following hyperbolic tangent black box based model

$$I_m(T) = (a_1 + a_2T)\tanh(V_b(b_1 + b_2T)) + V_b(c_1 + c_2T) \quad (2.3)$$

Where  $a_{1-2}$ ,  $b_{1-2}$  and  $c_{1-2}$  are the model coefficients,  $V_b$  is the bias voltage and  $T$  is the temperature. Figure 2.23a shows the IV characteristics of the 15  $\mu\text{m}$  mesa sensor with a line drawn marking the bias voltage used during the pulsed measurements. This bias voltage, as well as the current data at the five temperatures -50, -12.5, 25, 62.5 and 100  $^\circ\text{C}$  crossing the bias line can be used to extract the coefficients  $a_{0-1}$ ,  $b_{0-1}$  and  $c_{0-1}$ . The result is plotted against temperature in Figure 2.23b and is observed to be very linear with respect to temperature.

For the Schottky diode, the following 3rd order polynomial expression can be used to model the current temperature dependence.

$$I_m(T) = p_1T^3 + p_2T^2 + p_3T + p_4 \quad (2.4)$$

Where  $p_{1-3}$  are the extracted model coefficients and  $T$  is the temperature. The bias voltage for the Schottky diode is shown in Figure 2.23c. The expressions in (2.4) and (2.3) are valid in the vicinity of the marked bias lines. As with the mesa, the data points at  $V_b = 0.704$  V in Figure 2.23c can be used to find the coefficients  $p_{1-4}$ . The results is plotted versus temperature in figure 2.23d and is in contrast to Figure 2.23b not very linear with respect to temperature. Another approach to the Schottky modeling would be to use the real Schottky diode IV characteristics function as formulated in [11]

$$I_m(T) = I_s[\exp(qV_D/nkT) - 1] \quad (2.5)$$

where  $I_s = I_s(T^2)$ . However, an empirical polynomial model is simpler to use and works equally good for the purposes in this thesis.

To evaluate the sensitivity of the models a small voltage error can be added to the bias voltage and the corresponding data points can be used to extract new coefficients for the models in (2.3) and (2.4). Performing these steps with an error voltage of 50 mV result in the red curves plotted in Figure 2.23b and 2.23d. Clearly the mesa sensor is less affected by the error than Schottky diode. If the Schottky diode is characterized at 0.704 V and measures the ambient temperature of 300 K it corresponds to 20  $\mu\text{A}$ . If a 50 mV error occurs, the current increases to roughly 50  $\mu\text{A}$ . On the original current model, this current level corresponds to a temperature of about 338 K. Hence the voltage error translates to a temperature measurement error of almost 40  $^\circ\text{C}$ . In the case of the mesa sensor, the error translates to roughly 12  $^\circ\text{C}$ .

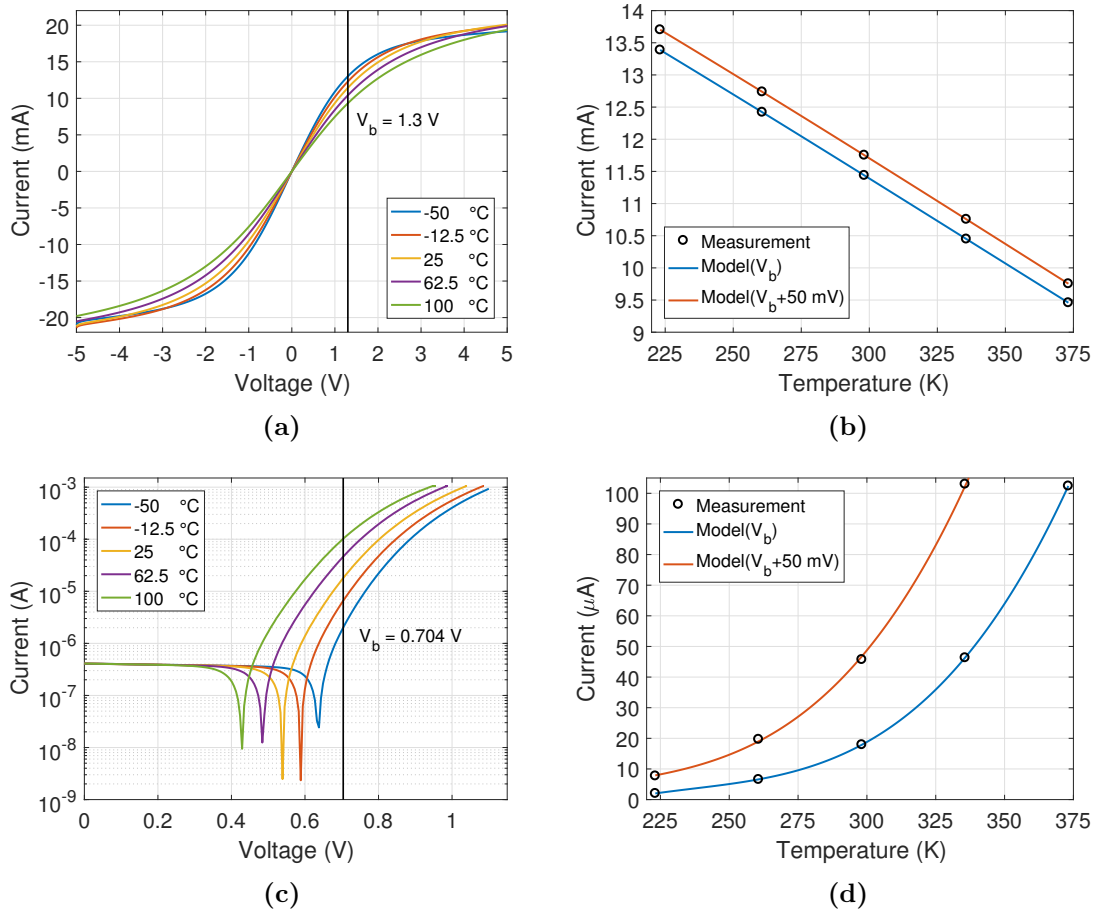


**Figure 2.23:** The 15 μm mesa and 25 μm Schottky IV characteristics with marked bias voltages (a), (c). Extracted  $I(T)$  model at bias and bias with perturbation for the mesa (b) and Schottky diode (d).

It is important to know what the sensitivity of the sensors looks like and how it behaves versus temperature. Such knowledge helps to select a good bias voltage and is critical for the analysis of the responses from different individuals. The sensitivity of the mesa sensor can be found by examining  $d/dT$  of (2.3). The derivative  $I'_m(T)$  can be written as

$$I'_m(T) = V_b c_2 + a_2 \tanh((b_1 + b_2 T) V_b) - V_b b_2 [\tanh((b_1 + b_2 T) V_b)^2 - 1] (a_1 + a_2 T) \quad (2.6)$$

It is clear from the mesa IV characteristics in Figure 2.10a that the peak sensitivity lies within the region 0.5 to 2 V. The function in (2.6) is plotted for bias voltages ranging from 0.22 to 2.2 V in Figure 2.24a. Clearly it can be seen that the magnitude of the sensitivity increases from 0.22 V and peaks around 1.32 V. It can also be seen that the sensitivity is fairly constant over all temperatures in the span at the voltage where the maximum occurs. Before this point, the slope of the curve is positive and after, the slope is negative, indicating a higher sensitivity for higher and lower temperatures respectively. These results are consistent with what can be seen in the IV measurement where the temperature "swing" peaks in the transition region. The point used for the measurements was 1.3 V and can be seen in Figure 2.24b to

be close to the maximum sensitivity point.

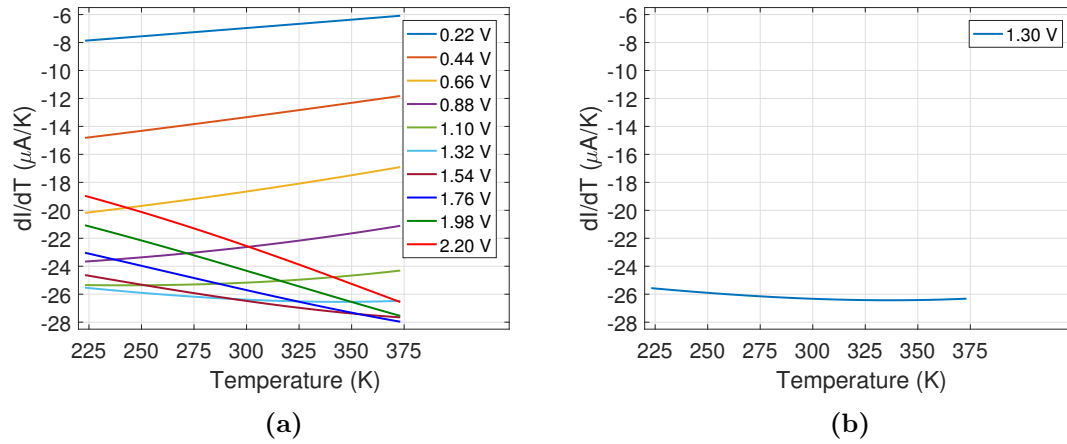


**Figure 2.24:** Sensitivity of the 15  $\mu\text{m}$  mesa sensor at  $V_b = 0.22\text{ V}$  to  $V_b = 2.20\text{ V}$  (a) and the measurement bias voltage  $V_b = 1.3\text{ V}$  (b).

For the Schottky model, the sensitivity is

$$I'_m(T) = 3p_1T^2 + 2p_2T + p_3 \quad (2.7)$$

This sensitivity varies as  $T^2$  and will therefore cause the response to vary significantly at different temperatures. This is verified by the measurements in Section 2.4.2 where Figure 2.18a shows a response magnitude approximately increasing from 2  $\mu\text{A}$  at  $-50\text{ }^\circ\text{C}$  to 32  $\mu\text{A}$  at  $100\text{ }^\circ\text{C}$  hence a 16 times increase. This can be compared to the approximate expected increase of 4 times which was measured by the mesa sensor in Figure 2.16b (the magnitude of the plot is considered in this case).

### 2.5.3 Temperature Estimation

The measured temperatures of the sensors can be evaluated by reading of the current response in the pulsed measurement and inserting the values in the models in Section 2.5.2. The following values are based on the 15  $\mu\text{m}$  mesa sensor at 2  $\mu\text{m}$  distance from the heater at 25  $^{\circ}\text{C}$ . From Figure 2.11a the starting current level can be read to be 11.48 mA and after 4.7 ms the current has decreased to 11.07 mA. From Figure 2.23b the starting current corresponds to a temperature  $T_0 = 297$  K and the current at 4.7 ms  $T_{4.7} = 312$  K. Hence, the temperature change is roughly 15  $^{\circ}\text{C}$  which is reasonable for 3.1 W of dissipated power in the heater. This power which is mainly transformed to heat is spreading in all three dimensions in the layer stackup and is also assumed to be strongly conducted in the metal access lines to the mesa heater.

For the 25  $\mu\text{m}$  Schottky diode with the same conditions, the starting current is given from Figure 2.11b to be 26.8  $\mu\text{A}$ . After 4.7 ms the current has increased to 38.61  $\mu\text{A}$ . From Figure 2.23d the starting current corresponds to a temperature  $T_0 = 313$  K and the temperature at 4.7 ms  $T_{4.7} = 328$  K. Hence, the temperature change is roughly 15  $^{\circ}\text{C}$ .

The reason for the offset value for the Schottky diode can be explained by the sensitivity in  $V_b$  for the I(T) model which was demonstrated in Section 2.5.2. The measured bias value was 0.707 V and the model value was 0.704 V (closest IV measurement point). Choosing  $V_b = 0.709$  V gives  $T_0 = 309$  K. Hence a small shift in the forward conducting threshold voltage  $V_T$  for the Schottky diode caused by e.g. a light source may therefore influence the measurement significantly.

The current change for the mesa sensor is roughly 410  $\mu\text{A}$  for a 15  $^{\circ}\text{C}$  temperature change. This gives about 27  $\mu\text{A}/\text{K}$  which can be compared to the sensitivity for the mesa sensor in Figure 2.24b. This leads to a value of 26  $\mu\text{A}/\text{K}$  which is very close to the measured value. Lastly it should be noted that even though the used IV model data was not from the individual doing the temperature measurement, it still resulted in very reasonable results.



# 3

## Low Noise Amplifier Study

When the temperature of the device is known, it can be used to take the necessary steps to acquire or maintain the desired performance. In this case the goal is to maintain the performance by mitigating the thermal effects in the device. The necessary actions can however only be taken if the state of the device can be predicted from the given temperature. Such predictions is ideally provided by models.

In this chapter, a study on three different LNAs is conducted to analyze the temperature and bias dependence of a number of key figures of merit. The study provides insight about the impact on these parameters from thermal effects and how it differs between processes. Furthermore, knowledge is provided about the possibilities and limitations of changing the bias. The chapter therefore lays the foundation for a temperature and bias characterization of the device which is needed for a dynamic bias control.

### 3.1 Performance Parameters

The design process of amplifiers is in general is often a trade-off between parameters which will improve/degrade at the cost of each other. The situation is similar for changing the bias and therefore all properties need to be monitored simultaneously to get the full picture. In the following section, relevant LNA figures of merit that measures noise, gain, power and linearity are reviewed. These key parameters will be studied for each LNA in later sections.

#### 3.1.1 Noise Figure

The Noise Figure (NF or F) is a figure of merit that describes the amount of noise generated in electronic devices. The definition of noise figure is the degradation of the Signal to Noise Ratio (SNR) at the reference source temperature of 290 K. This can be written as

$$F = \frac{S_i/N_i}{S_o/N_o} \quad (3.1)$$

where  $S_i$  is the input signal power,  $N_i$  is the input noise power,  $S_o$  the output signal power and  $N_o$  the output noise power. The noise powers are mostly dominated by

thermal noise and thus  $N_i$  and  $N_o$  can be written as

$$N_i = kT_0B \quad (3.2)$$

$$N_o = N_a + N_iG = N_a + kT_0BG \quad (3.3)$$

The input noise power in (3.2) is given by Boltzmann's constant  $k$  times the bandwidth  $B$  and reference temperature  $T_0$  (at 290 K). The output noise power in (3.3) is given by the input noise power times the gain  $G$  plus the added noise  $N_a$  from the device.  $N_a$  can be written as

$$N_a = kT_eBG \quad (3.4)$$

where  $T_e$  is the equivalent noise temperature of the device. The simplest model of the output signal  $S_o$  is the linear model. This model suggests that the output signal can be written as

$$S_o = S_iG \quad (3.5)$$

As seen from (3.4) and (3.1) The equivalent noise temperature and noise figure (F) are related in (3.1). Inserting (3.2), (3.3), (3.5) and (3.4) into (3.1) and simplify gives the relation as

$$T_e = T_0(F - 1) \quad (3.6)$$

#### 3.1.2 P1dB and Gain

An amplifier is in general a nonlinear device. A general non linearity may be simplified with a Taylor expansion according to

$$f(v(t)) = f(v_0) + \left. \frac{df}{dv} \right|_{v=v_0} (v - v_0) + \frac{1}{2} \left. \frac{d^2f}{dv^2} \right|_{v=v_0} (v - v_0)^2 + \frac{1}{3!} \left. \frac{d^3f}{dv^3} \right|_{v=v_0} (v - v_0)^3 + O^4 \quad (3.7)$$

For  $v_0 = 0$  it can be simplified to

$$f(v) = av + bv^2 + cv^3 \quad (3.8)$$

Where  $a$ ,  $b$  and  $c$  are the first second and third derivatives plus constants. For an input signal  $v(t) = A\cos(\omega t)$  the output can be evaluated as

$$\begin{aligned} f(v(t)) &= aA\cos(\omega t) + b(A\cos(\omega t))^2 + c(A\cos(\omega t))^3 \\ &= aA\cos(\omega t) + \frac{bA^2}{2}(1 + \cos(2\omega t)) + \frac{cA^3}{2}\cos(\omega t) + \frac{cA^3}{4}(1 + \cos(3\omega t)) \\ &= \frac{bA^2}{2} + \frac{cA^3}{4} + (aA + \frac{cA^3}{2})\cos(\omega t) + \frac{bA^2}{2}\cos(2\omega t) + \frac{cA^3}{4}\cos(3\omega t) \end{aligned} \quad (3.9)$$

Two additional harmonics occur at the output in (3.9). It can be seen that the fourth term with the  $A^3$  dependence is added to the fundamental desired frequency. This term is generally negative and therefore causes in band cancellation. As a consequence, the amplifier starts to compress and the amplification of any signal applied to the input is reduced.

A common measure for the level of compression is the P1dB point. The P1dB point is the point where the output power has decreased 1 dB from the amplifiers predicted linear output. Figure 3.1 shows a power sweep for an amplifier at a single frequency. The gain is defined in dB as  $G_{dB} = P_{out,dBm} - P_{in,dBm}$  and is constant in the linear region. The figure shows the P1dB point as the intersection between the linear output power minus 1 dB and the real output power curve. In this case the P1dB point is referred to the output.

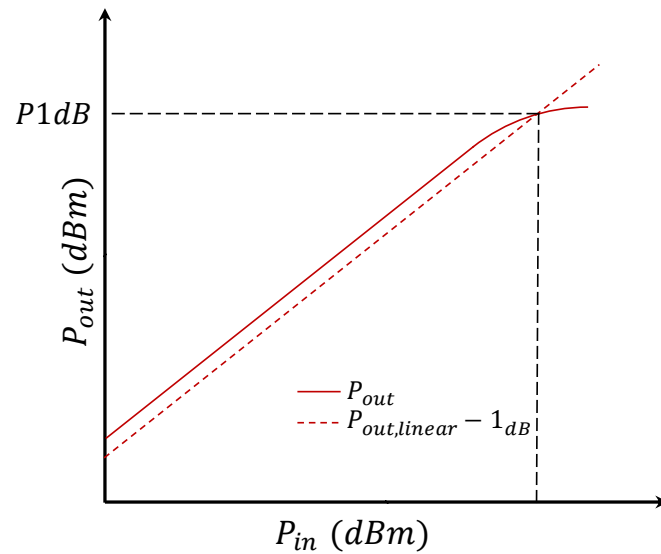


**Figure 3.1:** Amplifier compression curve with marked P1dB point referred to the output.

### 3.1.3 OIP3

If the input to (3.9) consist of two tones, additional products will appear on the output. For  $v(t) = A\cos(\omega_A t) + B\cos(\omega_B t)$  the output can be expressed as

$$f(v(t)) = a(A\cos(\omega_A t) + B\cos(\omega_B t)) + b(A\cos(\omega_A t) + B\cos(\omega_B t))^2 + c(A\cos(\omega_A t) + B\cos(\omega_B t))^3 \quad (3.10)$$

$$= i_a + i_b + i_c \quad (3.11)$$

Where

$$i_a = aA\cos(\omega_A t) + aB\cos(\omega_B t) \quad (3.12)$$

$$i_b = \frac{bA^2}{2}(1 + \cos(2\omega_A t)) + \frac{bB^2}{2}(1 + \cos(2\omega_B t)) - bAB[\cos((\omega_A + \omega_B)t) + \cos((\omega_A - \omega_B)t)] \quad (3.13)$$

$$i_c = \frac{cA^3}{4}\cos(3\omega_A t) + \frac{cB^3}{4}\cos(3\omega_B t) + \frac{3cA^2B}{4}[\cos((2\omega_A + \omega_B)t) + \cos((2\omega_A - \omega_B)t)] + \frac{3cB^2A}{4}[\cos((2\omega_B + \omega_A)t) + \cos((2\omega_B - \omega_A)t)] + \frac{3c}{4}(A^3 + 2AB^2)\cos(\omega_A t) + \frac{3c}{4}(B^3 + 2BA^2)\cos(\omega_B t) \quad (3.14)$$

The terms in (3.13) and first line in (3.14) represent harmonics of the two tones and are of little interest since they can easily be filtered away. The two terms in (3.12) and last line in (3.14) represent the desired signals and their compression terms respectively. The two middle lines in (3.14) represent the third order Intermodulation Distortion (IMD) products. The magnitude of these components limits the system since they contaminate the frequency spectra with frequency components which cannot easily be removed after the amplification. Consequently for a wideband signal, the third order IMD products cause in band distortion.

The Output third order Intercept Point (OIP3) is a measurement of the linearity of an amplifier. It is the value of output power, where the extrapolated linear magnitudes of the third order intermodulation distortion product and first order output power (the desired signal power) are equal. It can graphically be seen as the intersection point of the linear responses of the first and third order products.

Figure 3.2 shows the first and third products versus different input power levels and the linear intersection point. An amplifier with good linearity properties will generate small harmonics even for higher input power. This shifts the third order curve to the right in Figure 3.2 which results in a higher value of OIP3.

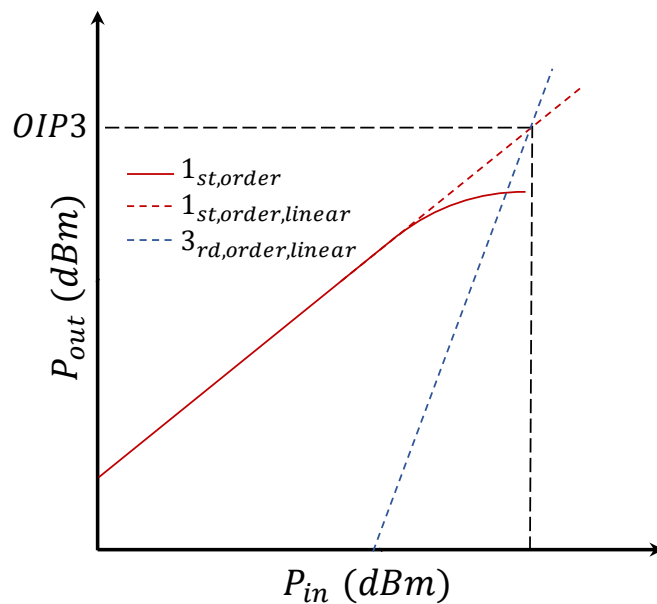


**Figure 3.2:** Amplifier third order intercept point referred to the output.

## 3.2 Measurement Setup

The same measurement setup is used to measure the following parameters of all three LNAs: S-parameters, noise figure, P1dB, gain (linear and at compression) and OIP3. The PNA-X from Keysight can be used to measure all these parameters with a single instrument.

The block diagram in Figure 3.3 shows the entire setup used for the LNA measurements. The DUT is placed in a closed nitrogen filled chamber in a probe station equipped with a thermal chuck (similar to the measurements setup in Chapter 2). The thermal chuck is the base of the chamber and can be set to temperatures ranging from  $-60\text{ }^{\circ}\text{C}$  to  $200\text{ }^{\circ}\text{C}$ . Two power supplies were used to provide bias supply voltages to the LNAs. Since all three amplifiers have two stages, it is in theory possible to use four power supplies in order to individually control the two gate and drain voltages for each amplifier. The Qorvo LNA did not however support such a setup so for the sake of simplicity and comparison, the setup with two PSUs was used for all three cases.

The power supplies and PNA-X are controlled with a GPIB interface by a control computer (PC) which runs a Visual Basic for Applications (VBA) based program that sets the bias supplies to a specific point and then runs the RF measurements with the PNA-X.

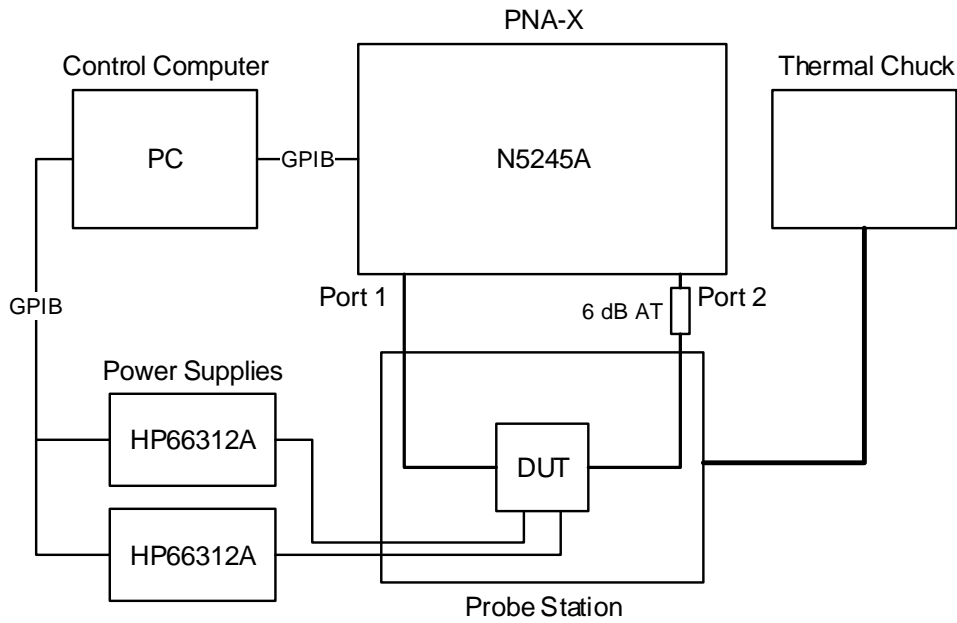


**Figure 3.3:** Measurement setup for the LNA measurements.

The PNA-X uses four channels to measure the LNA parameters. Channel 1 makes a S-parameter measurement with a linear frequency sweep from 1 to 10 GHz with 163 points and -15 dBm input power. Channel 2 measures the noise figure from 2 to 6 GHz with 53 points. Channel 3 measures the P1dB compression power level from 2 to 6 GHz at 53 points. At each frequency, the PNA-X makes an input power sweep from -20 to 2 dBm. In the ideal case, at some point during the power sweep, the device will have reduced its output power by 1 dB compared to the linear output power which is defined at an input power level of -20 dBm. Because the Qorvo LNA can output power levels that exceed the maximum acceptable power level into port 2 of the PNA-X, a 6 dB attenuator is added at the LNA output. The attenuation value is selected as low as possible to avoid unnecessary degradation of the noise measurement. In addition, an internal 10 dB attenuator is used at the receiver at port 2 in order to prevent receiver saturation during the power sweep.

Lastly, channel 4 of the PNA-X makes a two tone measurement to measure IMD products (described in Section 3.1.3). Two tones separated with  $\Delta f = 1$  MHz are centered around a center frequency  $f_c$ . This frequency is swept from 2 to 6 GHz with the  $\Delta f$  between the tones kept fixed. At each  $f_c$ , the receivers are tuned to all required IMD product frequencies to measure the power at each tone.

The two input tone powers are coupled at -20 dBm. This power level is low enough to avoid saturation of the receiver at port 2 (which risk to contaminate the measurement with nonlinear noise contributions from the PNA-X receiver). The tones are equal at the input of the device but may be unequal at the output because of gain variation versus frequency. The PNA-X therefore measures both the high and low side bands and calculates the dBm average which then is presented as the IMD tone power.

### 3.2.1 DUT Specifications and Settings

The basis for each LNA measurement is the bias voltage grid which consists of a sweep in the gate voltage  $V_g$  and drain voltage  $V_d$ . The start and end points of these variables have to be chosen to ensure that they cover the area of interest with enough points with reasonable drain current steps. For measurement time purposes the total number of bias points should not exceed approximately 250 points. The area of interest is the area between the pinch off voltage  $V_{pinch}$  and the gate voltage that results in a maximum compliance drain current for the device (at the nominal drain voltage  $V_{dq}$ ). The compliance drain current was in these cases set to 200 mA. A first guess of the upper limit of  $V_g$  is  $V_{g,200} = I_{200}/g_m$  where  $g_m$  is calculated as:

$$g_m = \frac{dI_d}{dV_g} \quad (3.15)$$

After the initial guess, a series of test measurements were conducted to find the appropriate bias grid for each LNA. The final values for the three LNAs are listed in Table 3.1.

	$V_{g,min}$	$V_{g,max}$	$V_{g,step}$	$V_{d,min}$	$V_{d,max}$	$V_{g,step}$	Points
Chalmers	-3.68 V	-2.08 V	0.08 V	5 V	15 V	1 V	231
Qorvo	-2.80 V	-2.15 V	0.08 V	5 V	20 V	1 V	224
UMS	-3.20 V	-2.06 V	0.06 V	5 V	15 V	1 V	220

**Table 3.1:** Bias measurement grids for the three LNAs.

The DUTs are two stage GaN MMIC low noise amplifiers for radar and electronic warfare applications [12]. Table 3.2 summarizes some specifications of the devices under test. The UMS LNA was designed using the UMS GH25-10 foundry service and the Chalmers LNA [13] using the Chalmers process [8]. The TGA2611 LNA is bought off the shelf from Qorvo and is shown in Figure 3.5. Note that only 4 pads are available for biasing ( $V_g$ ,  $V_d$  and 2xGND). All three LNAs have a nominal gate length of 0.25  $\mu\text{m}$ . Figure 3.4 shows the Chalmers LNA including bias, stabilization and matching networks to the two stages. Several self oscillating frequencies were detected on the gate and drain bias supplies for the Chalmers and Qorvo LNAs. Bias instability is mainly caused by the unpredictable impedance presented by the power supplies. It is further destabilized by connecting together the gate and drain voltages. These low frequency oscillations in the order of kHz and MHz were removed by connecting large capacitors ( $\mu\text{F}$ ) at the power supply terminals and by soldering small ceramic capacitors (nF) on the DC probes.

### 3. Low Noise Amplifier Study

LNA	Frequency Range (GHz)	Gain at 3 GHz (dB)	NF at 3 GHz (dB)	$I_{ds}$ (mA)	$V_{ds}$ (V)	$P_{out,sat}$ (dBm)	GW Stage 1/2 ( $\mu\text{m}$ )
UMS	2-6	21	2.4	80	10	25	4x100/4x100
Chalmers	2-6	15	1.5	80	10	20	8x50/8x50
Qorvo	2-6	28	1.0	110	10	29	N/A

**Table 3.2:** Specification of devices under test.

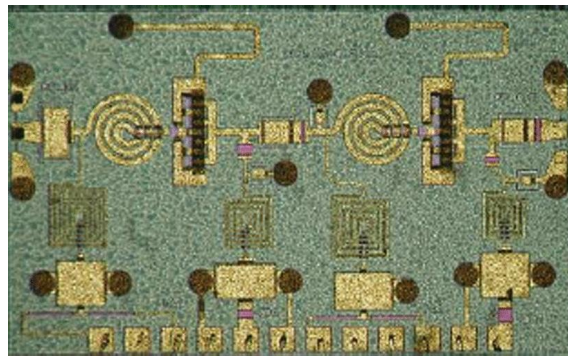


**Figure 3.4:** Chalmers S-Band MMIC LNA (size:  $2.3 \times 1.3 \text{ mm}^2$ )[13].

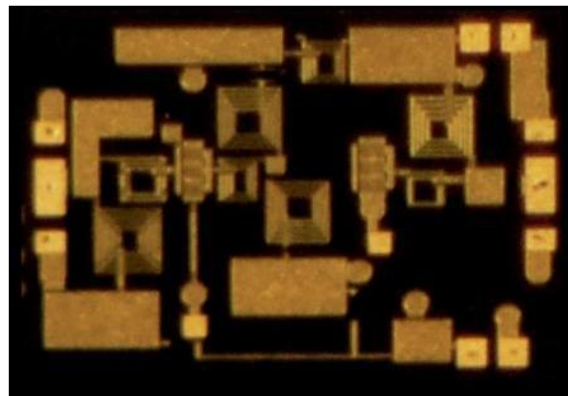


**Figure 3.5:** Qorvo S-Band MMIC LNA (size:  $2.1 \times 1.5 \text{ mm}^2$ )[14].



### 3.3 Measurement Results

In this section, the measurement results for the Qorvo, UMS and Chalmers LNAs are presented. The key performance parameters described in Section 3.1.1, 3.1.2 and 3.1.3 are measured for every bias point in Table 3.1 from the previous section.

#### 3.3.1 IV Curves

The IV characteristics shows the drain current dependence on the gate and drain voltage. The drain current dependence on temperature causes the quiescent current to change even if the bias voltages are kept constant. The change in current can mainly be attributed to changed electron mobility and threshold voltage  $V_T$  in the transistor. Moving the bias point means directly affecting the transistor properties. By extension this affects design conditions such as S-parameters which changes the optimal matching conditions and could also cause instability. Figure 3.6, 3.7 and 3.8 shows the IV characteristics of the three LNAs at -25 °C and 75 °C. As expected, for a given  $(V_d, V_g)$  the current decreases as the temperature increases.

The drift in the threshold voltage causes starting values to move more than other bias points versus temperature. As the temperature decreases, the LNA is more likely to oscillate. The reason for this is that the output stabilization network resistance decreases with temperature and will therefore present a lower impedance for the transistor which results in a decreased margin (or no margin at all) between the optimum output match  $\Gamma_L$  and the unstable region in the smith chart. The increased likely-hood of instability can also be seen from the expression of the maximum stable gain in the amplifier which can be expressed as

$$G_{Tmax} = \frac{|S_{21}|}{|S_{12}|} (K - \sqrt{K^2 - 1}) \quad (3.16)$$

Clearly in (3.16) if the gain increases, which is the case for lower temperatures, the stability factor  $K$  becomes smaller which means moving closer to potential instability.

As the oscillation conditions becomes satisfied, the LNA will swing at maximum amplitude which would cause such a bias point to make a jump in the drain current. The absence of these points in Figure 3.6, 3.7 and 3.8 indicate stable devices even at lower temperatures.

### 3. Low Noise Amplifier Study

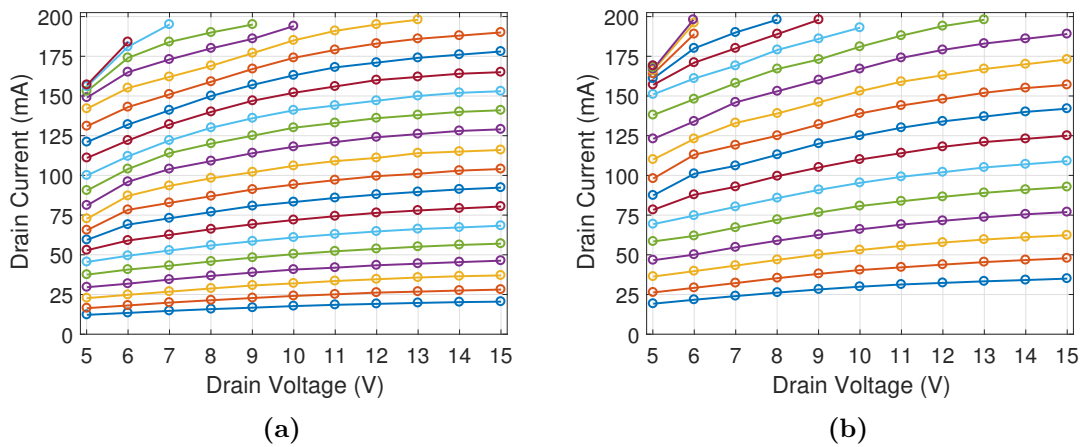


**Figure 3.6:** IV curves for the Chalmers LNA at 75 °C (a) and -25 °C (b) with  $V_{g,min} = -2.8$  V to  $V_{g,max} = -2.15$  V.

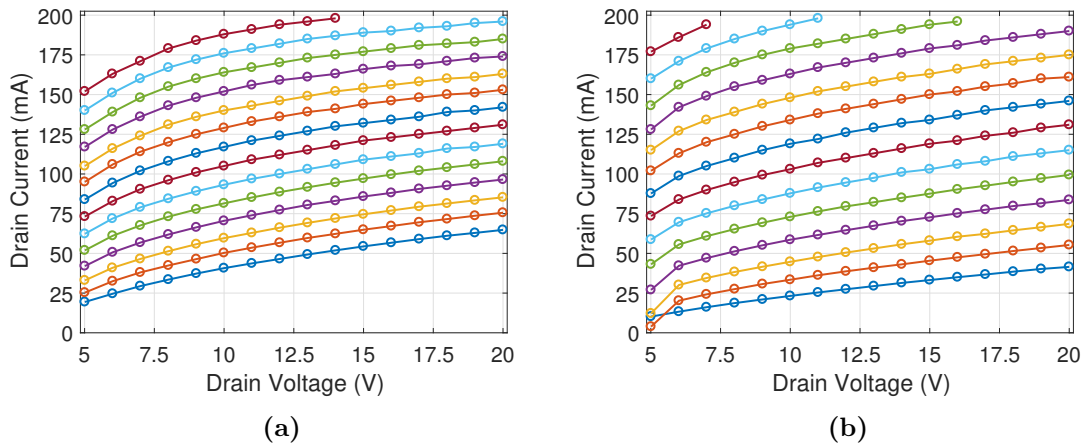


**Figure 3.7:** IV curves for the Qorvo LNA at 75 °C (a) and -25 °C (b) with  $V_{g,min} = -2.8$  V to  $V_{g,max} = -2.15$  V.

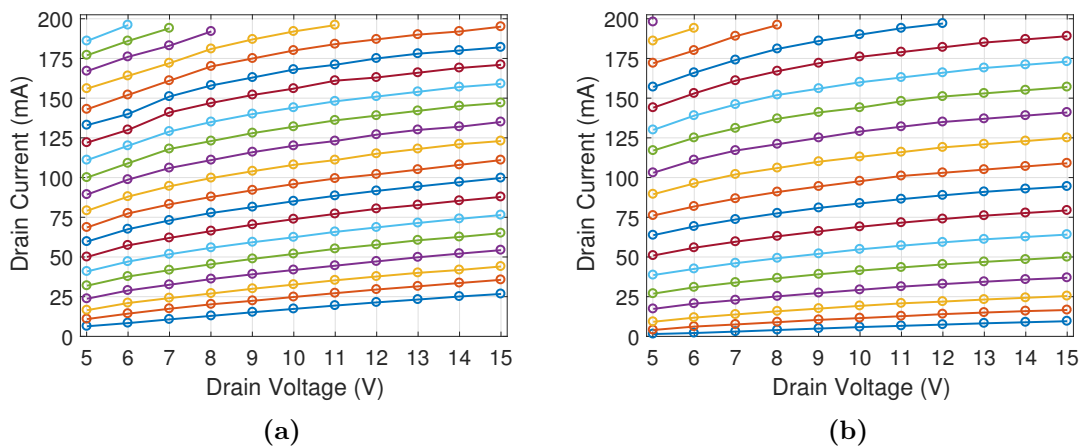


**Figure 3.8:** IV curves for the UMS LNA at 75 °C (a) and -25 °C (b) with  $V_{g,min} = -3.2$  V to  $V_{g,max} = -2.06$  V.

### 3.3.2 Bias Point Dependence

In this section, the temperature is kept constant and the LNA parameters are plotted as surfaces versus the bias points in Section 3.3.1. The surface plots are analyzed for a Continuous Wave (CW) frequency of 3 GHz and the measurement temperature is 25 °C.

The linear gain of the LNAs versus their respective bias grids is shown in Figure 3.9a (UMS), 3.10a (Chalmers) and 3.11a (Qorvo). It can be observed from the figures that the gain varies significantly with the bias point and mostly in the  $V_d$  direction. The Qorvo LNA exhibits the strongest  $V_d$  dependence and reaches about 30.6 dB at 20 V. The gain at the specified operating bias point ( $V_d = 10$  V,  $V_g = -2.5$  V) is 27.8 dB for this device. Hence at  $V_d = 20$  V the gain is almost 3 dB higher. For the Chalmers LNA the gain seems to decrease slightly at higher gate voltages apart from increasing with  $V_d$ . The gain at the specified operating point ( $V_d = 10$  V,  $V_g = -3.28$  V) is 15.5 dB. The UMS LNA in Figure 3.9a exhibits the weakest dependence on the drain voltage. The gain at the specified operating bias point ( $V_d = 10$  V,  $V_g = -2.78$  V) is 20.2 dB, and reaches a maximum value of 21.42 dB at  $V_d = 15$  V, hence a 1.2 dB increase. The DC power consumption  $P_{dc} = I_{ds}V_d$  is shown in Figure 3.9b (UMS), 3.10b (Chalmers) and 3.11b (Qorvo). All three LNAs dissipates about 3 W at  $V_d = 15$  V and it is clear from the plots that a higher gain is associated with a higher power consumption.

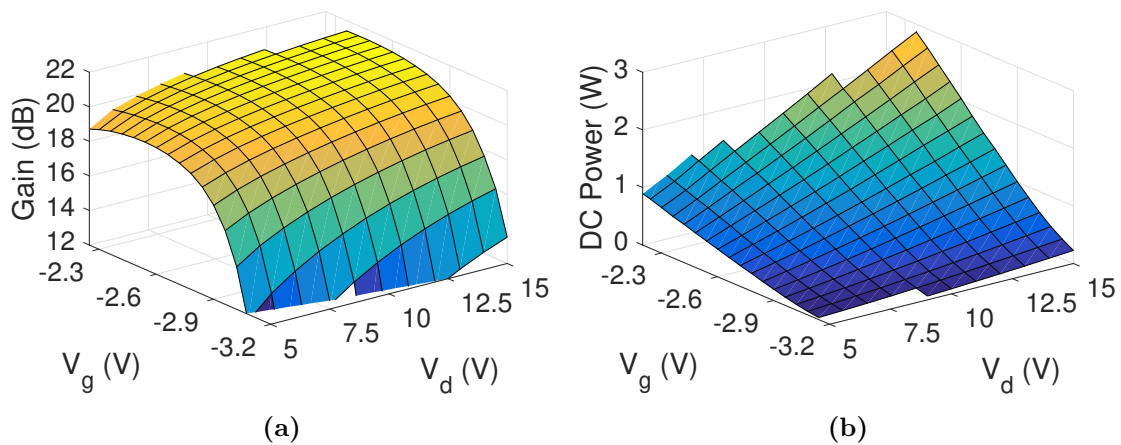


**Figure 3.9:** UMS LNA linear gain (a) and power consumption (b) versus  $V_d, V_g$  at 25 °C.

### 3. Low Noise Amplifier Study

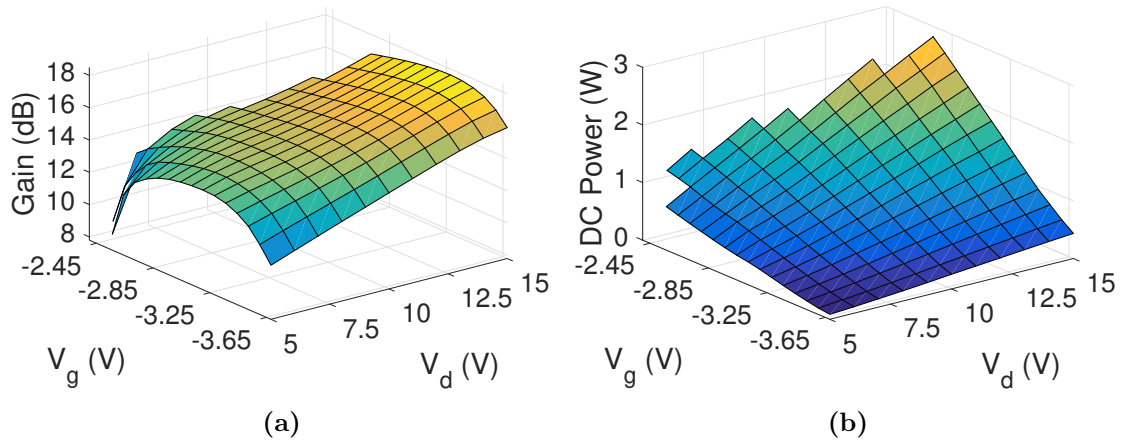


**Figure 3.10:** Chalmers LNA linear gain (a) and power consumption (b) versus  $V_d, V_g$  at 25 °C.

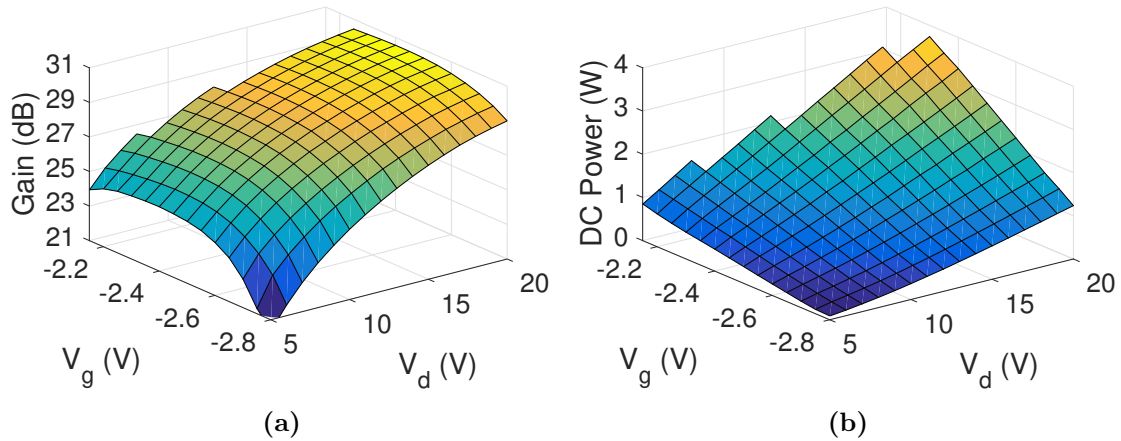


**Figure 3.11:** Qorvo LNA linear gain (a) and power consumption (b) versus  $V_d, V_g$  at 25 °C.

The next parameter to examine versus the bias point sweeps is the P1dB compression point which is shown in Figure 3.12a (UMS), 3.13a (Chalmers) and 3.14a (Qorvo). It can be observed from the figures that the P1dB point is more dependent on the drain current compared to the linear gain. This means a strong variation in the  $V_g$  direction and weaker in  $V_d$  direction. The Chalmers LNA however can be seen to saturate to a larger extent in the  $V_g$  direction compared to the others. The quiescent P1dB points for the UMS, Chalmers and Qorvo LNAs are 15.9, 14.4 and 20.3 dBm respectively. These values are as expected quite far from the  $P_{sat}$  values in Table 3.2. The measurement shows however that the P1dB point can be brought much closer to the  $P_{sat}$  point, resulting in a much larger linear power span for all three LNAs.

To reach each compression point in Figure 3.12a to 3.14a a power sweep was made as described in Section 3.2. If the measurement failed to reach a 1 dB compression level, the point taken as P1dB will be the closest measured value. Figure 3.12b, 3.13b and 3.14b shows the DeltaGain for the UMS, Chalmers, and Qorvo LNAs respectively. The figures shows the level of compression compared to the linear region for each point presented as P1dB. Ideally these figures should show a

plane at -1 dB if the measurement succeeded in reaching the P1dB point for all bias points. It can be seen that some points for the UMS LNA compressed less than 1 dB. A possible explanation for this is that these points are biased in such a way as to cause gain expansion at the end of the power sweep. Hence a larger power sweep would have been required for these points in order to reach the P1dB point.

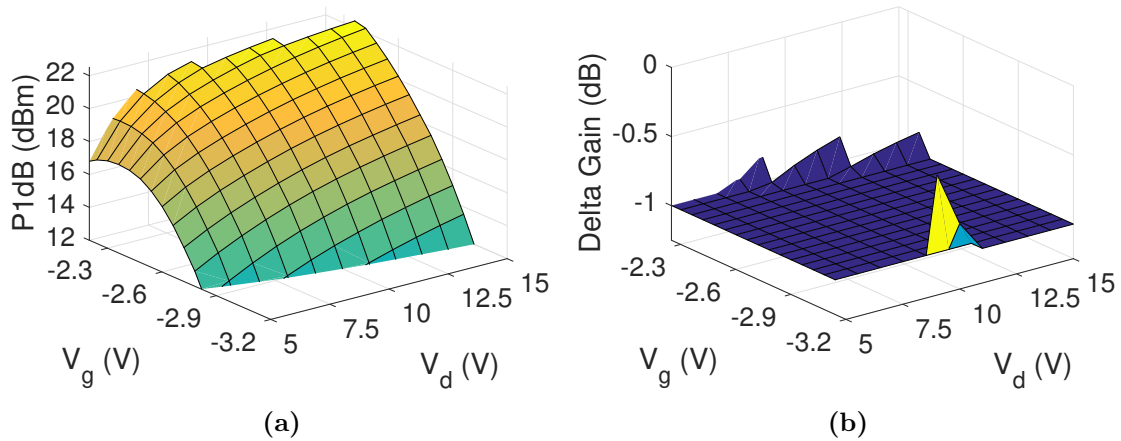


**Figure 3.12:** UMS LNA P1dB (a) and delta gain (b) versus  $V_d, V_g$  at 25 °C.

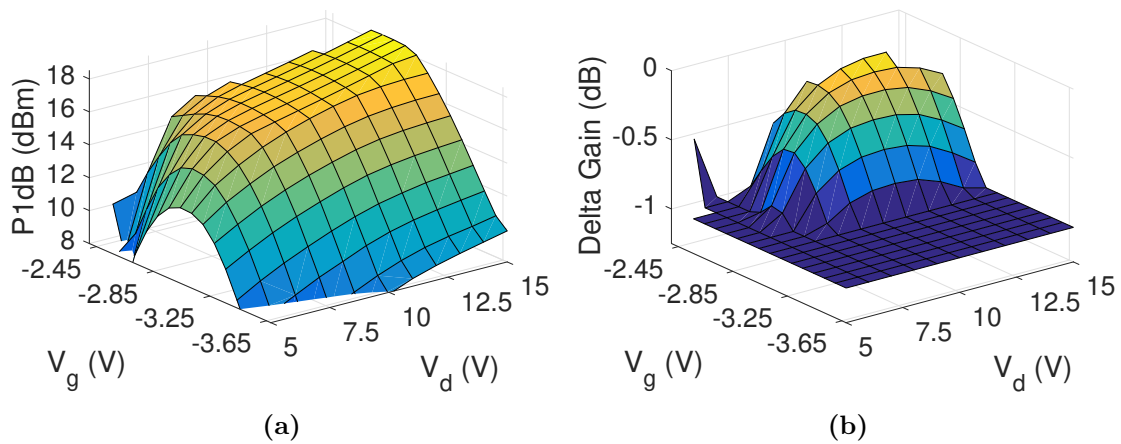


**Figure 3.13:** Chalmers LNA P1dB (a) and delta gain (b) versus  $V_d, V_g$  at 25 °C.

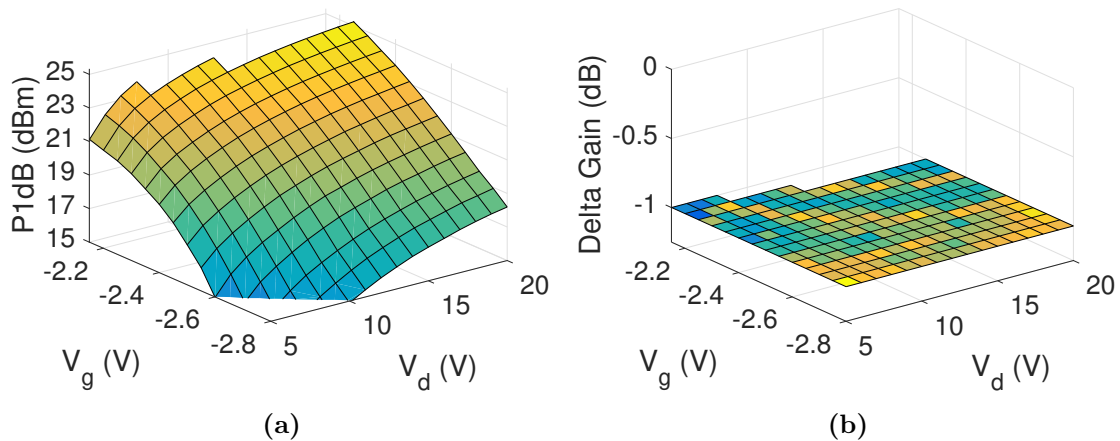


**Figure 3.14:** Qorvo LNA P1dB (a) and delta gain (b) versus  $V_d, V_g$  at 25 °C.

The last bias point dependence parameters to analyze is the OIP3 and NF measurements. The OIP3 measurements are shown in Figure 3.15a (UMS), 3.16a (Chalmers) and 3.17a (Qorvo). In general, it can be seen that the linearity performance increases with larger  $V_d$  values. This is expected since increasing  $V_d$  will bias the transistors in a manner that ensures a sinusoidal drain current waveform. This is also known as class A type operation which is the most linear type of operation. The strongest dependence of the OIP3 measurement can however be seen in the  $V_g$  direction. The maximum values of the UMS, Chalmers and Qorvo LNAs can be found from the figures to be 34.2, 32.6 and 34.8 dBm. This can be compared with the quiescent point values which are 27.1, 24.7 and 31.4 dBm respectively. Clearly bias points with higher OIP3 values are available although the Chalmers and UMS LNA measurements shows a more noisy result which makes the uncertainty larger. It can also be concluded that like the gain surfaces, higher linearity values also results in higher power consumption for all three LNAs.

The noisier results can be explained from Section 3.3.1 where it can be seen that the UMS and Chalmers LNAs have more points close to current compliance levels where the uncertainty is higher. Furthermore, using more measuring points also results in capturing more noise.

The noise figure of the LNAs are shown in Figure 3.15a (UMS), 3.16a (Chalmers) and 3.17a (Qorvo). It can be observed from the figures that the NF increases fast as the LNA approaches the pinch off gate voltage level. Note that the x and y axes have been swapped in these figures for visualization purposes. The quiescent noise figure points for the UMS, Chalmers and Qorvo LNAs are 2.5, 2.2 and 1.3 dB respectively. The figures indicate that it is possible to decrease the NF of the LNAs with about 0.2 to 0.4 dB. The minimal value can be seen to occur at a low  $V_d$  and maximum  $V_g$  values. Finally, it can also be observed that the Chalmers LNA exhibits a stronger dependence on the drain voltage compared to the UMS and Qorvo LNAs.



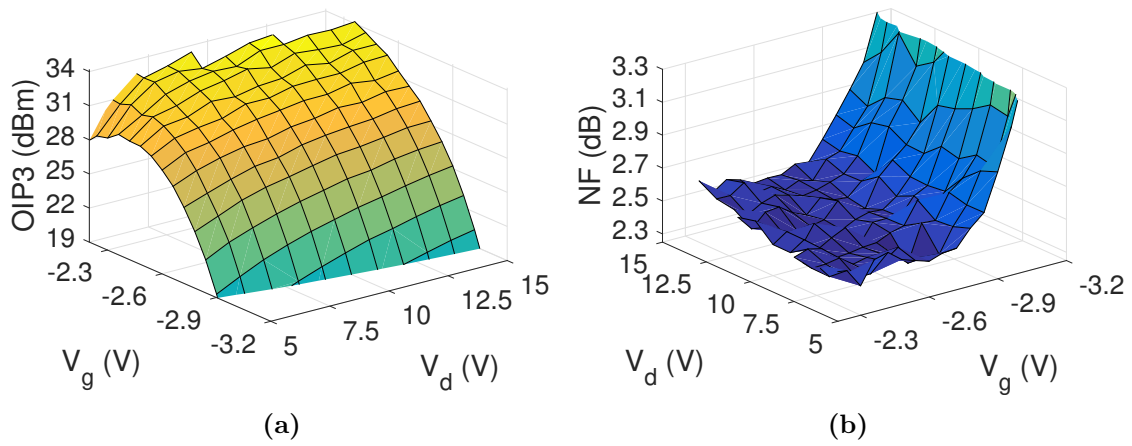


Figure 3.15: UMS LNA OIP3 (a) and noise figure (b) versus  $V_d, V_g$  at 25 °C.

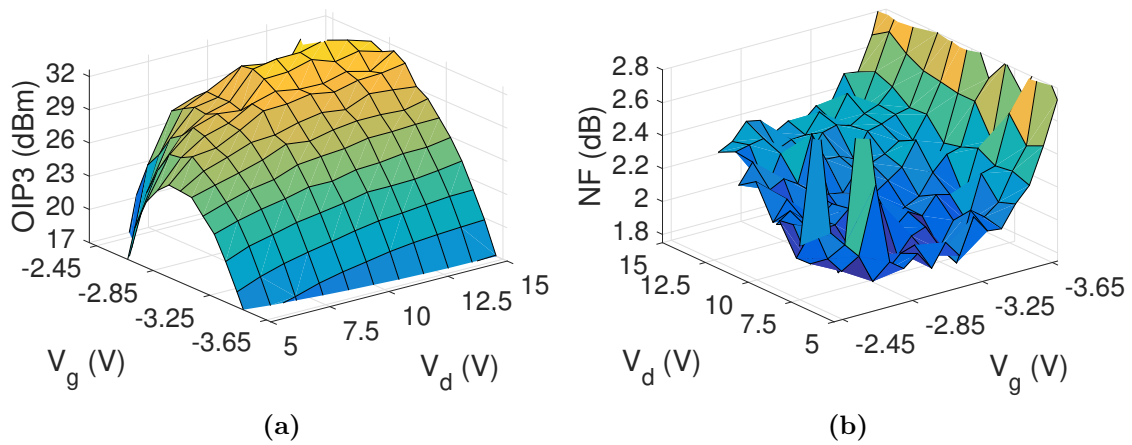


Figure 3.16: Chalmers LNA OIP3 (a) and noise figure (b) versus  $V_d, V_g$  at 25 °C.

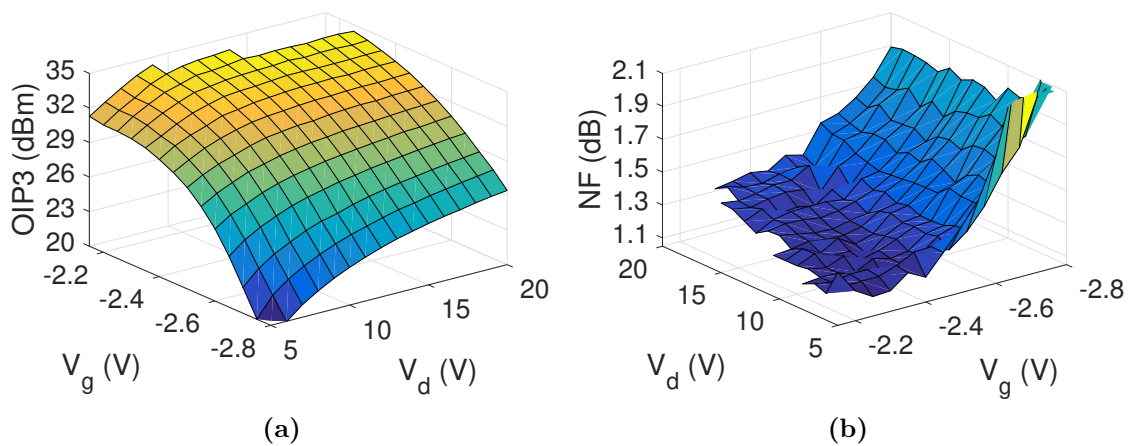


Figure 3.17: Qorvo LNA OIP3 (a) and noise figure (b) versus  $V_d, V_g$  at 25 °C.

### 3.3.3 Temperature Dependence

In this section, the drain voltage  $V_d$  is kept constant at 10 V and the LNA parameters are plotted as surfaces versus the gate voltage and five temperatures. As with the previous surfaces, the plots are analyzed for a CW frequency of 3 GHz.

The temperature dependence of the linear gain of the LNAs is shown in Figure 3.18a (UMS), 3.19a (Chalmers) and 3.20a (Qorvo). Although to a different extent, in all three cases, the gain decreases with increasing temperature. It can be expected since transistor S-parameters are a function of temperature and will therefore change. This will result in new optimum matching conditions which will not be satisfied with the current matching networks in place (which were designed at a constant temperature). The gain usually suffers most from the resulting miss match situation. The gain of the UMS, Chalmers and Qorvo LNAs are reduced by approximately 2.5, 1.5 and 3 dB respectively. Hence the gain is reduced by half for the Qorvo LNA and is most stable for the Chalmers LNA.

The behaviour of the P1dB points in Figure 3.18b (UMS), 3.19b (Chalmers) and 3.20b (Qorvo) is different. It can be observed to be fairly constant versus temperature for the UMS and Qorvo LNAs. A 1 dB reduction can be noted for the Chalmers LNA as well as a local minima at 50 °C which is believed to be a measurement error caused by e.g. calibration uncertainty. It is clear from these measurements that studying the absolute output power properties with P1dB is complex. Since P1dB is a strong function of the linear properties of the LNA, the linearity temperature dependence has a great influence. Hence it is possible that the LNA has the ability to output a very high power even though the 1 dB compression occurs early. A better measurement for the absolute power properties of the LNAs is the  $P_{sat}$  value which is the power output level when the gain is reduced to zero.

A possible explanation of the constant behaviour of the P1dB measurement is that the temperature dependence of the pinch off voltage is counteracting the expected drain current reduction which would decrease the P1dB point. The measurement is more easily seen in the power sweep curves for the specified frequency (3 GHz) and quiescent bias point for each LNA. The power sweep for each temper-

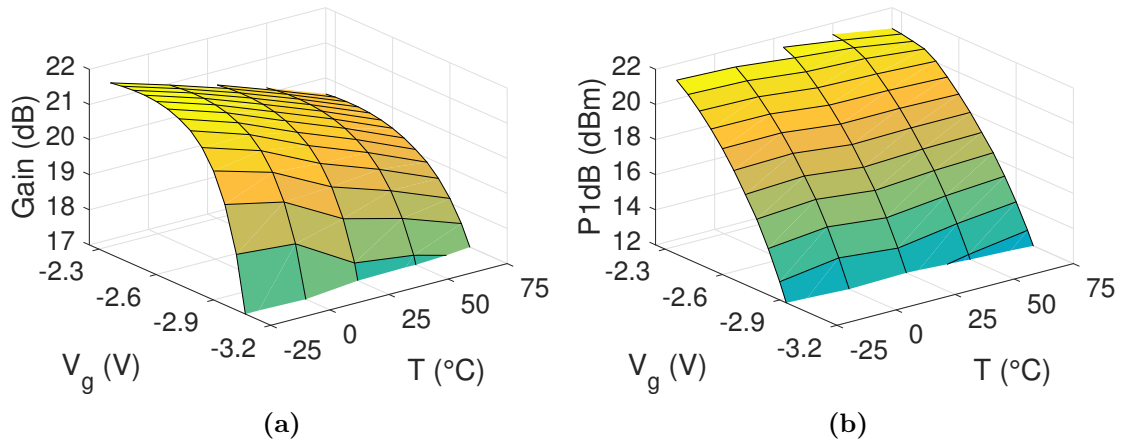


**Figure 3.18:** UMS LNA linear gain (a) and P1dB (b) versus  $V_g, T$  at  $V_d = 10$  V.



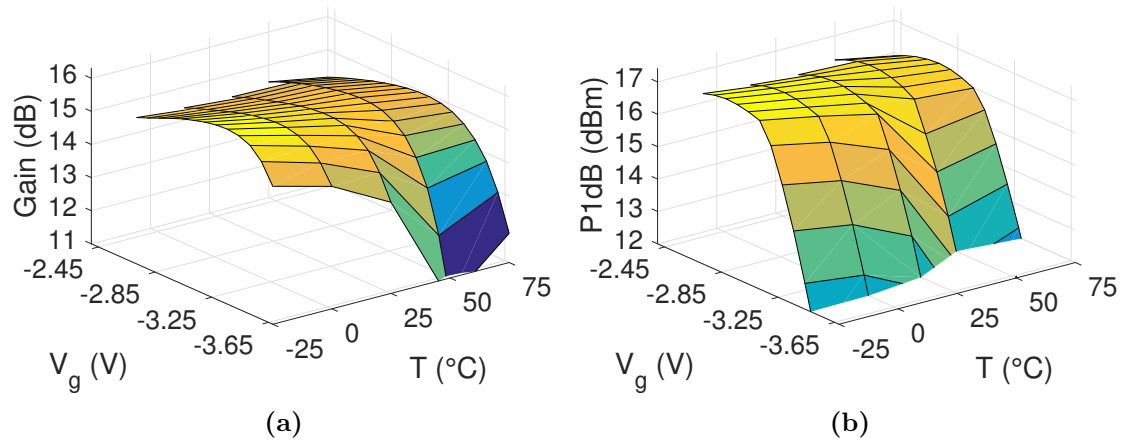


**Figure 3.19:** Chalmers LNA linear gain (a) and P1dB (b) versus  $V_g, T$  at  $V_d = 10$  V.

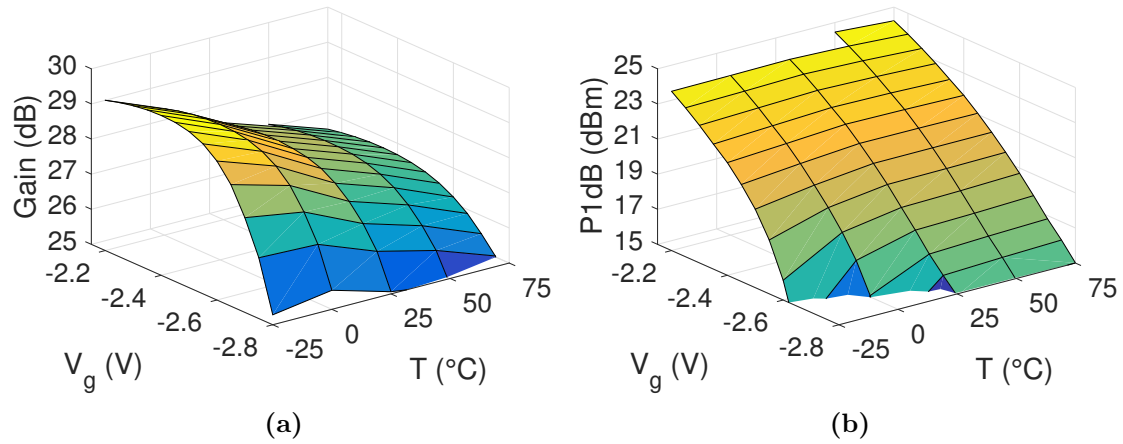


**Figure 3.20:** Qorvo LNA linear gain (a) and P1dB (b) versus  $V_g, T$  at  $V_d = 10$  V.

ature can be seen in Figure 3.21a (Qorvo) and 3.21b (Chalmers) where the P1dB point is marked in each curve. Clearly the overall power level is reduced with temperature as can be predicted from the reduced gain. Furthermore, the P1dB point can be seen to vary very little for the Qorvo LNA whereas it is reduced by several dB for the Chalmers LNA. It is believed that this difference is due to changed linearity properties for the Chalmers LNA which is caused by changing the bias point. The bias point is defined in terms of drain current  $I_d$  and drain voltage  $V_d$  and the drain current is reduced for the Chalmers LNA. This can be seen in Figure 3.22b which shows a reduction of roughly 30 mA in the drain current for the Chalmers LNA when the temperature is increased from  $-25$  °C to  $75$  °C. This will shift the class of operation towards a class AB mode which is more nonlinear compared to the class A mode. The P1dB point which is a point where nonlinear effects start to become significant therefore decreases, indicating a reduced linear power span.

It can be seen in Figure 3.22a that the drain current is maintained versus temperature for the Qorvo LNA and consequently, the P1dB point is affected to a much smaller extent compared to the Chalmers LNA.

### 3. Low Noise Amplifier Study

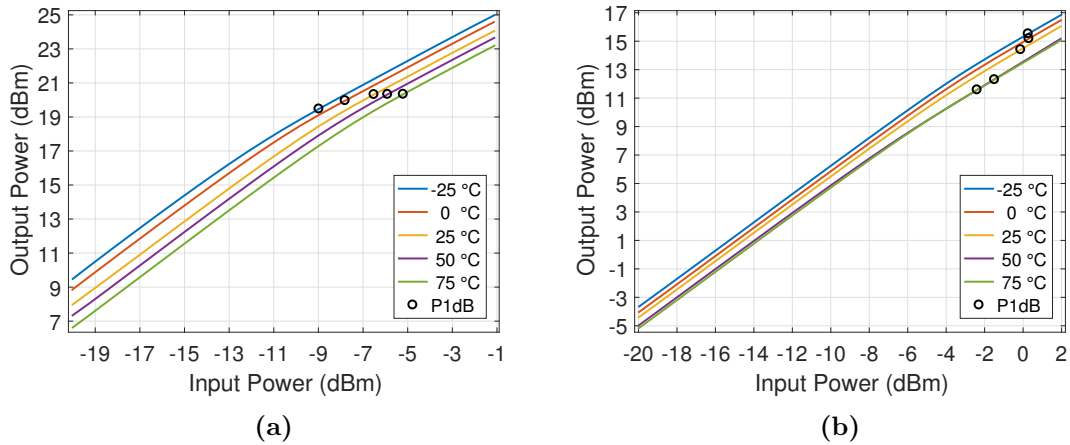


**Figure 3.21:** Quiescent point power sweep curves at different temperatures at 3 GHz for the Qorvo (a) and Chalmers (b) LNAs.

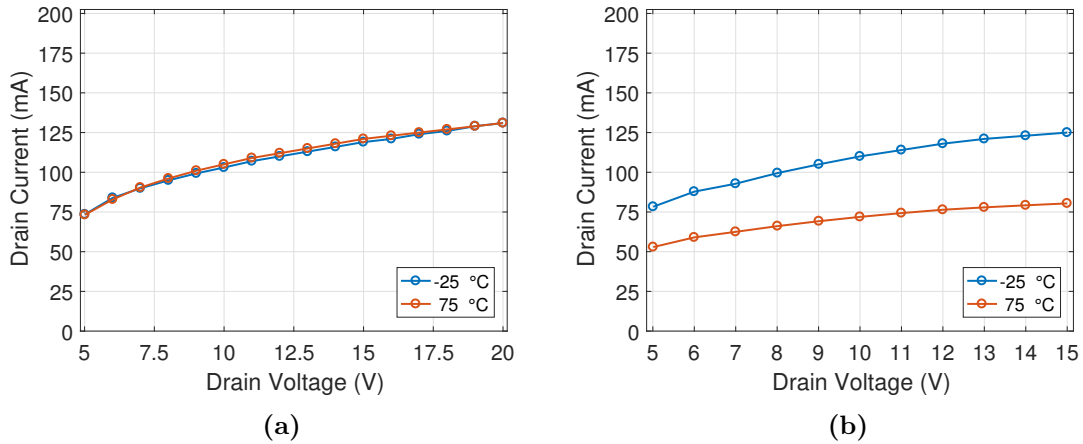


**Figure 3.22:** Drain current at  $-25\text{ }^{\circ}\text{C}$  and  $75\text{ }^{\circ}\text{C}$  for the Qorvo (a) and Chalmers (b) LNAs.

The final parameters to be evaluated versus temperature are the noise figure and OIP3 measurements. Figure 3.23a, 3.24a and 3.25a shows the OIP3 of the UMS, Chalmers, and Qorvo LNAs respectively. It can be observed from these plots that linearity decreases in the order of 1 to 2.5 dB from  $-25$  to  $75\text{ }^{\circ}\text{C}$ . A reduction in OIP3 is a direct consequence from a reduction in the desired tone power level as described in Section 3.1.3. Therefore, apart from seeing a reduction for the UMS and Chalmers LNAs, a reduction in the OIP3 can also be seen for the Qorvo LNA. This is more apparent at higher  $V_g$  values and is a difference compared to the P1dB measurement.

Lastly, the noise figure is shown in Figure 3.23b (UMS), 3.24b (Chalmers) and 3.25b (Qorvo). Note that the x and y axes have been swapped in these figures for visualization purposes. It can be seen that the thermal noise is strongly affected by increasing temperatures as expected. The UMS has the largest increase in noise figure followed by the Chalmers and Qorvo. The latter is seen to increase to 1.5 dB from the quiescent point value of 1.3 dB. A possible measure to prevent this increase of 0.2 dB is to bias the LNA in the minimum value of 1.1 dB in Figure 3.25b.

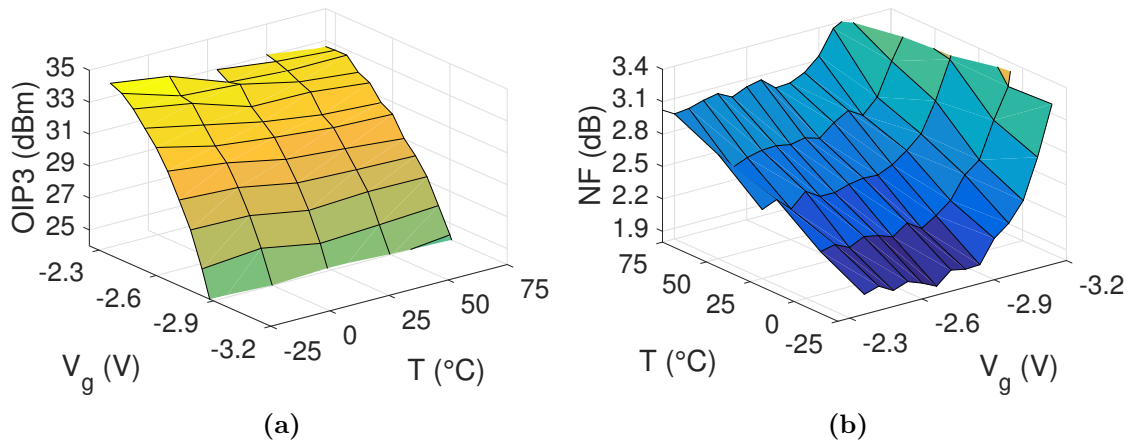


Figure 3.23: UMS LNA OIP3 (a) and NF (b) versus  $V_g, T$  at  $V_d = 10$  V.

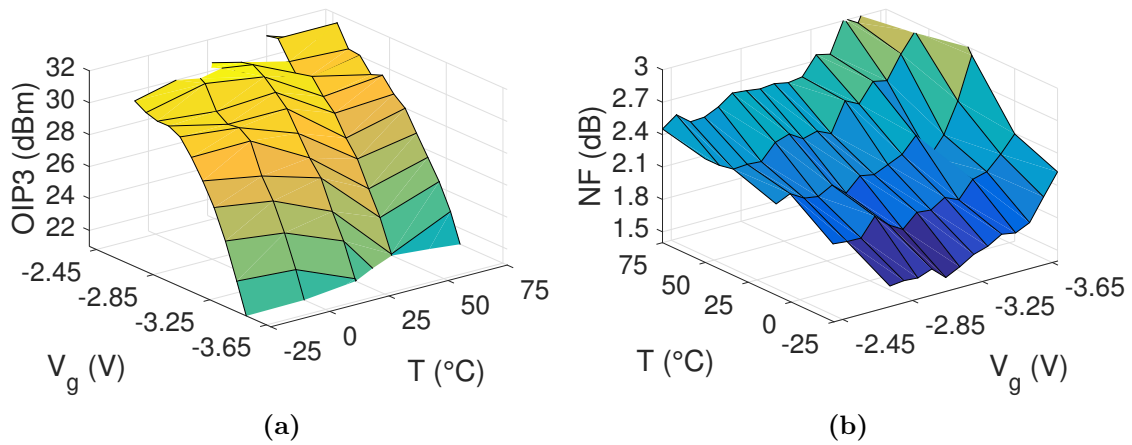


Figure 3.24: Chalmers LNA OIP3 (a) and NF (b) versus  $V_g, T$  at  $V_d = 10$  V.

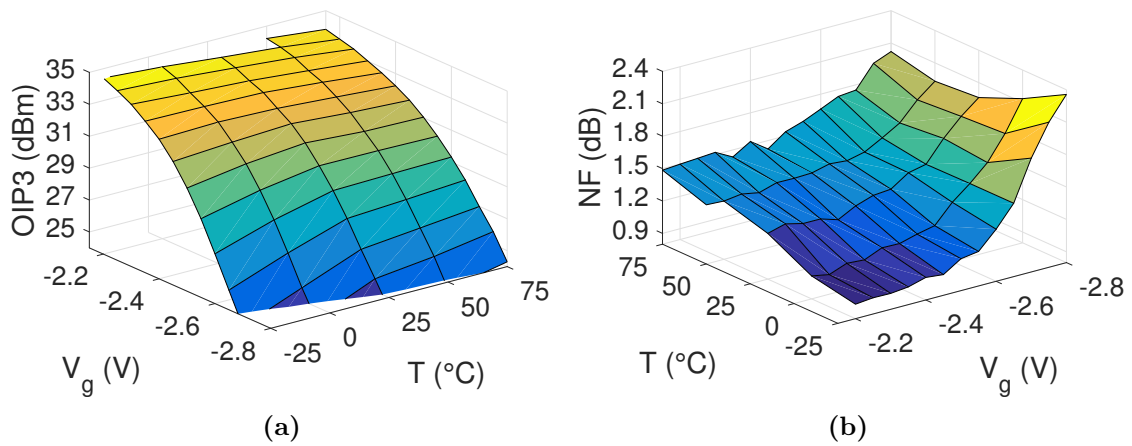


Figure 3.25: Qorvo LNA OIP3 (a) and NF (b) versus  $V_g, T$  at  $V_d = 10$  V.

### 3.3.4 Temperature and Bias Dependence

A problem with surfaces in Section 3.3.3 is that the temperature dependence for the full bias grid cannot be visualized simultaneously but is limited to a single drain voltage. The surfaces in Section 3.3.2 on the other hand shows the entire bias grid but do not take into account the temperature dependence. In this section the figures in Section 3.3.2 are transformed to contours and are plotted for  $-25$ ,  $25$  and  $75$  °C. Because the noise figure surfaces are not very smooth surfaces, they are not shown as contours in this section.

The gain showed the largest degradation with temperature in Section 3.3.3, this should also be manifested in the contours. Figure 3.26 shows the linear gain contours of the UMS, Chalmers, and Qorvo LNAs. The chosen contour levels is the quiescent gain at  $25$  °C except for the UMS LNA. This is because the quiescent gain level was not available at  $75$ °C for this LNA and is therefore chosen  $0.5$  dB lower. Two things should be noted in Figure 3.26. Firstly, the constant gain contour lines moves towards higher  $V_d$  with increasing temperature and secondly, the largest steps are taken by the UMS LNA followed by the Chalmers and Qorvo LNAs. It is clear from the figure that in order to maintain the gain level over temperature, control over the drain voltage is critical.

In contrast, gate voltage control alone is sufficient for the P1dB contour lines which is shown in Figure 3.27. The previous observations from Section 3.3.3 are verified in this figure which shows that the P1dB movement (temperature dependence) is fairly small and that the Chalmers LNA moves more compared to the other two. A similar behaviour can be seen for the OIP3 contour lines in Figure 3.28, hence, the movement is fairly small. The Chalmers and Qorvo LNAs show a difference in tendency. The constant contour line for the Chalmers LNA can be seen to move upwards for the Chalmers LNA whereas it moves to lower  $V_g$  values for the Qorvo LNA. This is believed to be due to the small OIP3 and P1dB temperature dependencies which would require too small steps in the  $V_g$  direction to be able to distinguish a clear pattern.

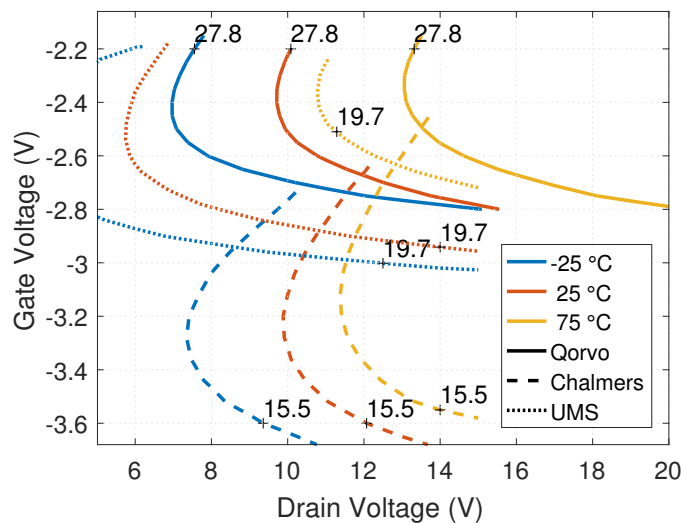


**Figure 3.26:** Contours of constant gain versus temperature for the three LNAs.

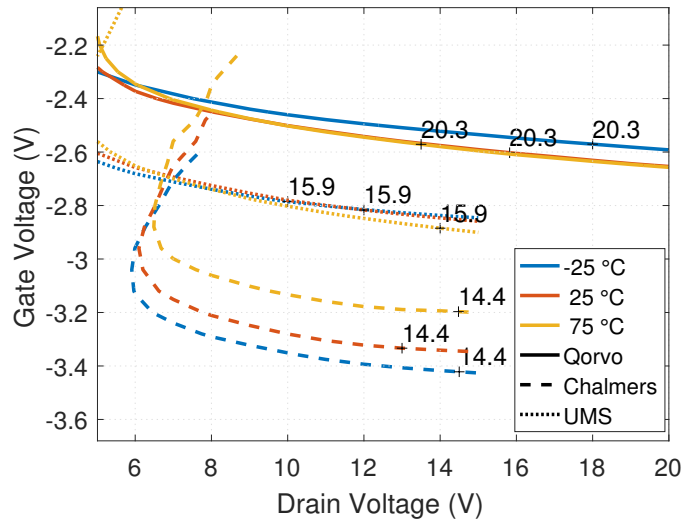


Figure 3.27: Contours of constant P1dB levels versus temperature for the three LNAs.

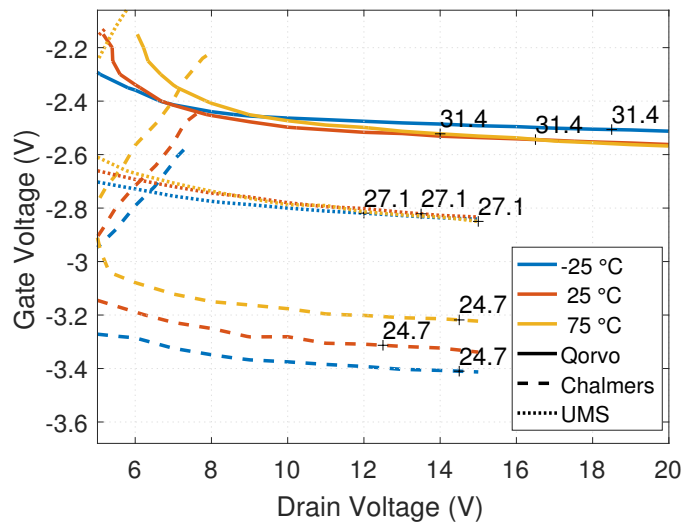


Figure 3.28: Contours of constant OIP3 levels versus temperature for the three LNAs.

### 3.3.4.1 Dynamic Bias Demonstration

It is clear from Figure 3.26 that the constant level contour lines merely move to other locations in the grid when the temperature changes. It is therefore possible to have a certain parameter unaffected by temperature changes by moving the bias point to the same location that the contour line moved to. In fact, infinite number of solutions are possible since any point on the contour line gives the same parameter value. This results in an optimization problem whose result will determine which of the possible solutions gives the best overall performance of the LNA.

The following example shows how dynamic bias control can be used to keep the gain level constant over temperature. Note that this example is not the optimum solution with respect to all parameters. The optimal control case is not handled since it involves setting restrictions and goals which are strongly application dependent.

Figure 3.29 shows the same contours for the Qorvo LNA as in Figure 3.26 but with additional marked bias points. The quiescent bias point (BQ) can be seen to be at the specified gain level as expected. As the temperature goes from  $-25\text{ }^{\circ}\text{C}$  to  $75\text{ }^{\circ}\text{C}$  with the LNA biased at quiescent point, the gain is expected to decrease with increased temperatures. If the bias point rather follows the proposed path in Figure 3.29, starting from B1 at  $T = -25\text{ }^{\circ}\text{C}$ , to B2 at  $T = 25\text{ }^{\circ}\text{C}$  etc, the gain will remain constant.

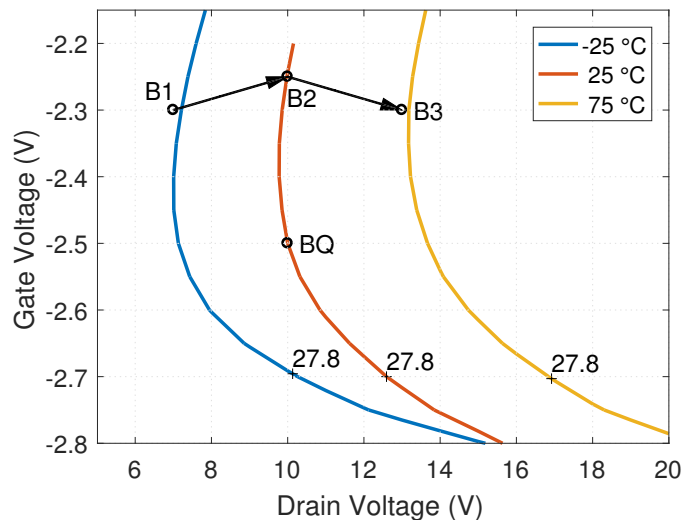


**Figure 3.29:** Gain contours of Qorvo LNA with bias control path (B1, B2 and B3) and quiescent point gain (BQ).

The result of following the path in Figure 3.29 can be seen in Figure 3.30 (right column). The figure clearly shows a constant gain level versus temperature as expected. The left column shows the constant bias situation hence the case where the bias voltages are not changed. Clearly the changes for OIP3 and P1dB are quite small as was concluded from Figure 3.27 and 3.28. For the controlled gain case however, these parameters are increased approximately 3 dB with a slightly larger variation between the bias points.

Furthermore, as could be predicted in Section 3.3.2, a higher gain is also associated with a higher power consumption. In this case, the gain control case requires

a peak increase power consumption of 1.1 W.

Lastly, it can be seen how the noise figure is unaffected or even lower by following the specific bias control path compared to the constant bias case. This means that the Signal to Noise Ratio (SNR) in the receiver will not be degraded as a result of controlling the gain. On the contrary, it is more likely to be significantly improved because of the enhanced linearity properties which resulted from the dynamic bias control.

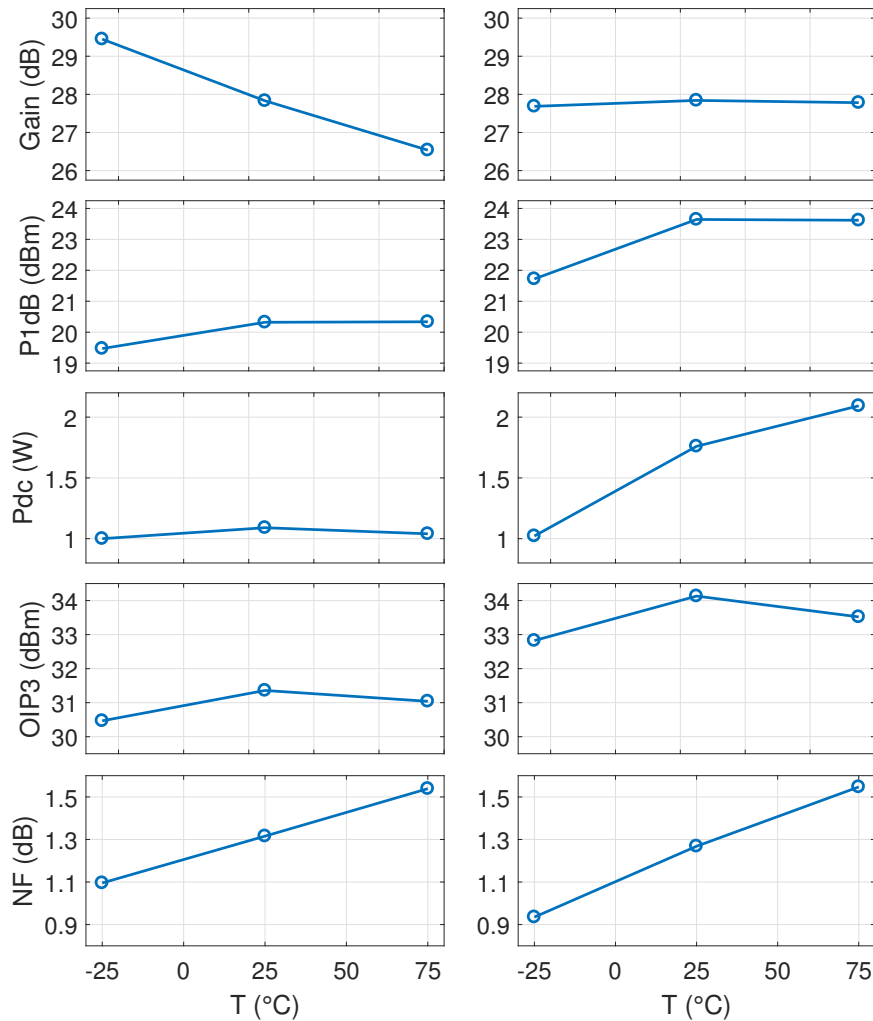


**Figure 3.30:** Uncontrolled gain (left column) and controlled gain (right column).

If a reduced power consumption is desired, parameters such as noise figure will deteriorate significantly and in the end trade offs between parameters have to be made. It is also possible to have different modes of operation which are suitable for different scenarios in e.g. a radar application. If the environment of operation demands moderate performance from the radar, the LNA can operate in a low power mode which provides moderate SNR with a controlled gain. Such a mode of operation might however be insufficient in a more demanding environment such as situations involving jamming signals and targets with small radar cross sections. The RF Pulse Measurement section demonstrates one of these situations. In such

situations, the noise level is expected to increase from nonlinear contributions in the LNA as well as the presence of foreign RF signals. Therefore, maximum OIP3 is required to minimize these contributions. This is achieved by maximizing  $V_g$  and  $V_d$  which also will maximize the gain. This control of the bias would correspond to a high performance mode of operation which, because of the much higher DC power consumption, can only be used temporarily.

## 3.4 RF Pulse Measurement

It was demonstrated in Section 3.3.4.1 how dynamic bias control can be used to prevent temperature degradation or even enhance the performance of any of the four LNA parameters. As a consequence, the control scheme therefore becomes applicable to a wide range of applications and situations. In this section, another example of an application of dynamic bias control is presented where the method is applied to the LNA recovery time study in [12]. In this study, the recovery time of the gain is measured after subjecting the LNA to a high power Radio Frequency (RF) pulse.

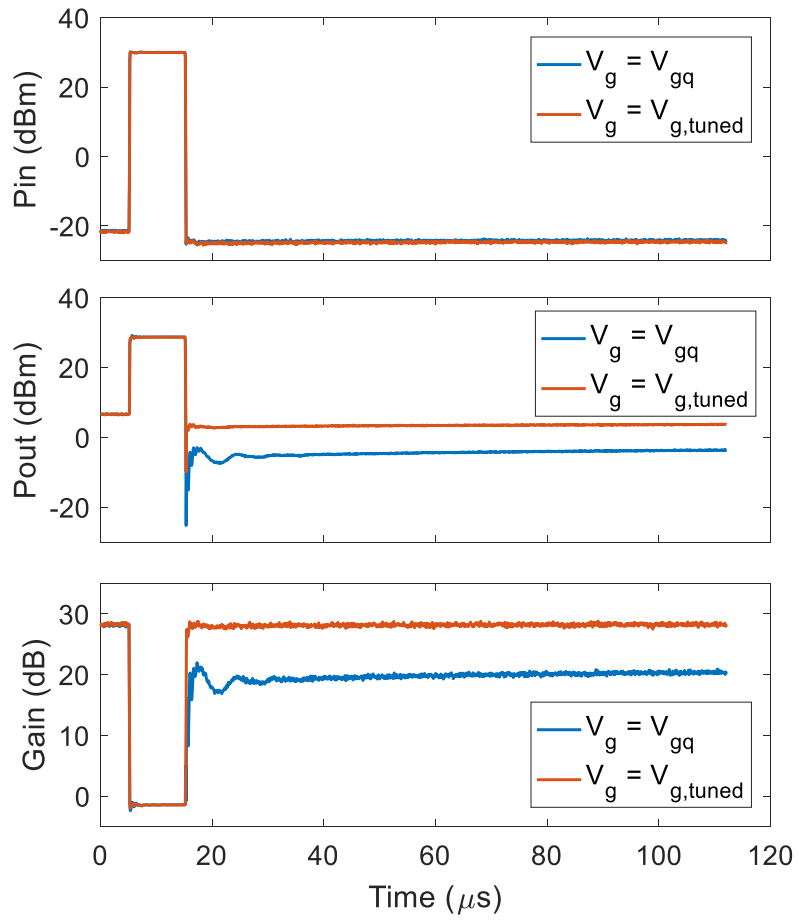
It was pointed out in Chapter 2 how trapped electrons reduces the current in the channel between the AlGaIn-GaN layers. In the case of the Gallium Nitride (GaN) High Electron Mobility Transistor (HEMT), the trapped electrons will create a negative potential relative the 2-DEG and consequently decreases the number of carriers in the 2-DEG, and hence the drain current. Furthermore, it is clear from the gain figures in 3.9a to 3.11a that a decrease in  $I_{ds}$  ( $V_g$  in the figures) will reduce the gain drastically as the voltage reaches the pinch of voltage.

Figure 3.31 shows a high power RF pulse measurement for the Qorvo LNA with the gate value at the quiescent voltage and a tuned value (-2.24 V). The peak input pulse power (top plot) is 30 dBm during a pulse width of 10  $\mu$ s. This level of input power (which is close to the OIP3 level) drives the LNA far into compression and the gain reduces to 0 dB as can be seen in the bottom plot. It can also be seen that after the pulse, the gain for  $V_{gq}$  does not recover to the initial value until several hundreds of  $\mu$ s after the pulse has ended. To ensure a total recovery, the pulse period was set to 100 ms. During this time the receiver gain is at most 10 dB lower than expected and the receiver cannot operate. On the contrary, for the tuned gate bias, it can be seen that the gain is unaffected after the pulse has ended.

The reason is that the electrons trapped during the pulse manages to decrease the current close to pinch off levels (where the gain is most sensitive) for the  $V_{gq}$  bias. This is not the case for the tuned bias where the current is offset to a larger value before the pulse starts and therefore has some margin to the region where the gain starts to decrease.

This is consistent with the first of the conclusions drawn in [12] which state that the gain recovery time can be mitigated at the cost of increased power consumption and increased noise figure. Figure 3.17b shows that increasing the gate voltage leads to a lower noise figure (1.32 to 1.27 dB). Hence mitigating the gain recovery will not necessarily come at the cost of increased noise figure for the Qorvo LNA.





**Figure 3.31:** High power RF Pulse Measurement with tuned and quiescent gate voltage.



# 4

## Summary and Conclusions

Important summarized results and conclusions are presented in the following bullet paragraphs:

- The bias dependence measurements showed improvement possibilities for the gain, output power, linearity and noise figure. The enhancement and control of these parameters are possible without increasing the noise figure compared to the static bias case. In the region beyond  $V_{pinch}$ , the dependence is different for some parameters. The P1dB and OIP3 parameters showed a strong dependence of  $V_g$  and the gain showed a stronger dependence of  $V_d$ . A notable process dependence was seen for the gain and noise figure. The UMS LNA showed the most invariant behaviour of  $V_g$  and  $V_d$ . Control over both  $V_d$  and  $V_g$  is required to be able to improve all four parameters.
- The LNA temperature dependence measurements showed that increasing temperatures in general deteriorates the performance parameters differently. The gain and noise figure showed the largest performance decline. The largest gain decrease was noted for the UMS and Qorvo LNAs. The reason for the process differences lies within material properties and remains to be investigated further. The OIP3 and P1dB measurements showed the smallest temperature decline due to a maintained drain current caused by the drift in  $V_{pinch}$ .
- The movement of the contour lines is related to the level of degradation and how the device responds to a change in bias. Because of this, the gain contour steps of the UMS LNA were larger compared to the Chalmers and Qorvo LNAs. Using the contour plots, a certain parameter can be kept constant by following the steps taken by the contour lines. Improved performance comes at the cost of increased power consumption and trade offs between parameters have to be made. The increased power demand could amplify the thermal effects and cause a thermal runaway. It is also possible to have different modes of operation which are suitable for different scenarios. Preventing gain recovery effects is an example of such a mode.
- Both a Schottky diode and mesa resistor can be used to determine the on-chip temperature. However, the mesa resistor sensor is easier to use in practice since the conditions for operation are less stringent. The mesa sensor showed reasonable start and stop temperatures for a pulsed measurement. The Schottky diode was not able to predict the correct start temperature. This is because it requires a very stable bias voltage as well as raw characterization data (I versus V,T) for every

individual. Variation in these factors caused larger problems for the Schottky sensor regarding sensitivity compared to the mesa sensor. For both sensors, an uncertainty is introduced when the same IV data is used as model basis for all individuals. In the ideal case, each sensor should undergo a calibration procedure where an IV temperature characterization is made and a model is extracted and used to determine the measured temperature for the specific sensor.

- The best region to bias the mesa sensor for temperature measurements was at the end of the linear region. This is mainly to avoid self heating effects but also to achieve maximum sensitivity with a temperature dependence as constant as possible. With the proposed  $I(T)$  models, the mesa resistor gives a very linear  $I_m(T)$  function which was less sensitive to voltage perturbations compared to the Schottky diode. Furthermore,  $I'_m(T)$  was confirmed to be very linear over a large temperature span. The Schottky  $I_m(T)$  was a nonlinear function and it was more sensitive to voltage perturbations. The current sensitivity was also nonlinear which was evident in the temperature dependence measurements. The Schottky IV characteristics indicate that  $V_T$  is more linear with respect to temperature. The Schottky diode is therefore believed to be a much better thermal sensor when driven with a constant current source.
- It is crucial that the sensor is scaled down to give a quiescent current that falls inside an appropriate current range of the current waveform analyzer. There are no indications that this would lower the relative current sensitivity of the sensors and it means that even smaller sensors, which would be more practical to implement on a chip, should be possible to use.
- Light was observed to affect the measurement. These effects can cause a systematic error if the light environment for the IV characterization and operation environment is different. In the ideal case, the light environment during calibration and later application is the same and is preferably a controlled environment where the illumination of the GaN structure is minimized.
- The power pulses in the heaters gave a clear response from the mesa sensor for distances 2-400  $\mu\text{m}$ . The error in sensitivity is very small for the mesa sensor which was proved by the responses from the 2 and 5  $\mu\text{m}$  sensors. A way to minimize the sensitivity error is to make an IV characterization for every individual and evaluate (2.6) and then tune  $V_b$  to make (2.6) as equal as possible for all sensors. The Schottky sensitivity issues made a comparison of the magnitude of the response at different distances meaningless. A similar delay however validates the mesa measurements. For distance dependent measurements, the mesa sensor is overall better suited.
- A lower temperature change was measured by the sensor when the measurement was performed at lower temperatures. This is believed to be due to increased thermal conductivity in the GaN and SiC layers. Because of this, the heat is spread much easier in all directions in the GaN layers and the overall temperature in the proximity of the heater (where the sensor is 2  $\mu\text{m}$  away) is lowered.
- The modeling of the response made it possible to analyze the lateral transient heat spread in the layer structure. The coefficients  $\tau_{1-2}$  and  $A_{1-2}$  were related

to the heat transfer in the GaN and SiC layers respectively. The primary path of heat transfer was seen to occur in the GaN layer. It was observed that the thermal conductivity was higher in the SiC layer compared to the GaN layer. It is believed also that the thermal conductivity degrades faster in the GaN layer compared to the SiC layer.

It is possible that more exponential terms can give more information about the contributions to the third time constant. The first two time constants were observed to increase with distance and temperature. A sensor placed further away might therefore experience increased response time and it might take longer time to reach a steady state. In a bias control situation this would lead to increased time delay in the control loop.

- From a practical perspective the higher current response of the mesa sensor is more practical in a real system since it requires less amplification. The mesa sensor is also easier to implement since it does not require a gate metal. It is also likely that the sensor can be made even smaller and be placed even closer to heat spots on the chip.

#### 4. Summary and Conclusions

---

# 5

## Future Work

The LNA study has shown that the concept works in theory and the initial measurements in the GaN sensor study have shown very promising results. Future work is summarized in the following bullet paragraphs:

- The raw measurement data for each LNA data is limited to discrete points and suffers from measurement uncertainties. The usage of this data for dynamic bias control purposes is unpractical and cannot be used for more precise control. It is desirable to extract multivariable models from the measured data. Furthermore, the models can be combined to find expressions for the SNR in the receiver. The SNR is the most important parameter in radar situations and is directly related to the Probability of Detection (PD) which then also can be predicted and controlled.
- Nonlinearities in the LNA can increase the noise power significantly at higher input power levels. The LNA measurements have shown that the linearity can be significantly improved and it is therefore of high interest to investigate if the SNR can be improved by dynamic bias control. This can be done by doing a RF multitone measurement where the power on the input tones are swept from a low to a high level and the output SNR is measured. This measurement is then performed at appropriate bias points selected from the OIP3 measurement.
- The issue of increased heat levels from the increased DC consumption needs to be studied carefully. The heating elements can produce long duration heat pulses. These heaters can be placed close to a device and heat the DUT continuously. The temperature should then be measured continuously as the device compensates for the degradation caused by the pulses. Such a setup can give insight into how much the DUT self heating further degrades the performance. In addition, long term reliability studies have to be performed to investigate the long term effects of the dynamic bias control scheme.
- The temperature of the sensor needs to be measured independently with a separate measurement device. This is preferably done with a heat camera that captures the transient sequence of the pulsed measurement.
- The increased response time of the sensor is important from a control perspective. It needs to be investigated how this affects the time to reach a steady state. This can be done by performing measurements with the large heating elements over very long distances and longer pulses.

- The GaN layer structure can be set up in a simulation program such as COMSOL Multiphysics. The transients measurements can then be compared with electrothermal simulations which should show a similar behaviour of the heat spread.
- The modeling of the current response can be further improved. The expression for the response is made of a step function and sequence function. The step function handles the propagation delay but it makes the expression discontinuous and the transition is not smooth which results in a bad curve fit in the transition region. It is believed that other delay functions can improve this. In addition, it should be investigated if adding more exponential terms is meaningful.
- It is also of interest to model the the current response of the Schottky diode. The results regarding the propagation delay and heat spread in the layers should be consistent with the results from the modeling of the mesa response. Furthermore, the Schottky measurements should be performed with a voltage measurement when operating the diode with a constant current. It is possible that the diode can outperform the mesa resistor when operated this way.
- Lastly, it is of interest to understand to what extent light disturbances impacts the temperature measurement results. A more careful study needs to be made that investigates under what conditions a light disturbance becomes significant. Such a study should also look into expose time and recovery time of the current.



# Bibliography

- [1] W. Gautier, W. Gruener, R. Rieger, and S. Chartier, “Broadband Multifunction AESA Front-Ends : New Requirements and Emerging Technologies”, *2016 46th European Microwave Conference (EuMC)*, pp. 334–337, 2016.
- [2] C. Dual and P. Beams, “To demonstrate the resulting output power vs NF trade-off, Fig. 7.2.3 compares the TX front-end (FE) OP”, *2017 IEEE International Solid-State Circuits Conference (ISSCC)*, pp. 128–130, 2017.
- [3] S. Zehir, O. D. Gurbuz, A. Kar-Roy, S. Raman, and G. M. Rebeiz, “60-GHz 64- and 256-Elements Wafer-Scale Phased-Array Transmitters Using Full-Reticle and Subreticle Stitching Techniques”, *IEEE Transactions on Microwave Theory and Techniques*, vol. 64, no. 12, pp. 4701–4719, 2016, ISSN: 00189480.
- [4] Y. Noh, Y. H. Choi, and I. Yom, “Ka-band GaN power amplifier MMIC chipset for satellite and 5G cellular communications”, *Proceedings of the 2015 IEEE 4th Asia-Pacific Conference on Antennas and Propagation, APCAP 2015*, pp. 453–456, 2016.
- [5] S. Nuttinck, B. K. Wagner, B. Banerjee, S. Venkataraman, E. Gebara, J. Laskar, and H. M. M. Harris, “Thermal analysis of AlGaIn-GaN power HFETs”, *IEEE Transactions on Microwave Theory and Techniques*, vol. 51, no. 12, pp. 2445–2452, 2003, ISSN: 00189480.
- [6] S. Wang, F. Xue, and A. Q. Huang, “Physics Understanding of High Temperature Behavior of Gallium Nitride Power Transistor”, *2016 IEEE 4th Workshop on Wide Bandgap Power Devices and Applications (WiPDA)*, pp. 324–327, 2016.
- [7] C. Florian, T. Cappello, D. Niessen, R. P. Paganelli, S. Schafer, and Z. Popovi, “Efficient Programmable Pulse Shaping for X-Band GaN MMIC Radar Power Amplifiers”, *IEEE Transactions on Microwave Theory and Techniques*, vol. 65, no. 3, 2017.
- [8] M. Südow, M. Fagerlind, M. Thorsell, K. Andersson, N. Billström, P.-Å. Nilsson, and N. Rorsman, “An AlGaIn/GaN HEMT-based microstrip MMIC process for advanced transceiver design”, *IEEE Transactions on Microwave Theory and Techniques*, vol. 56, no. 8, pp. 1827–1833, 2008, ISSN: 00189480.
- [9] S. Gustafsson, Jr-Tai Chen, J. Bergsten, U. Forsberg, M. Thorsell, E. Janzen, and N. Rorsman, “Dispersive Effects in Microwave AlGaIn/AlN/GaN HEMTs With Carbon-Doped Buffer”, *IEEE Transactions on Electron Devices*, vol. 62, no. 7, pp. 2162–2169, Jun. 2015, ISSN: 0018-9383.
- [10] I. Angelov, H. Zirath, and N. Rorsman, “A new empirical nonlinear model for HEMT and MESFET devices”, *IEEE Transactions on Microwave Theory and Techniques*, vol. 40, no. 12, pp. 2258–2266, 1992, ISSN: 00189480.

- [11] S. K. Cheung and N. W. Cheung, “Extraction of Schottky diode parameters from forward current-voltage characteristics”, *Applied Physics Letters*, vol. 49, no. 2, pp. 85–87, 1986, ISSN: 00036951.
- [12] O. Axelsson, N. Billström, N. Rorsman, and M. Thorsell, “Impact of trapping effects on the recovery time of gan based low noise amplifiers”, *IEEE Microwave and Wireless Components Letters*, vol. 26, no. 1, pp. 31–33, Jan. 2016, ISSN: 15311309.
- [13] N. Billström, J. Nilsson, A. Tengs, and N. Rorsman, “High performance GaN front-end MMICs”, in *European Microwave Week 2011: "Wave to the Future", EuMW 2011, Conference Proceedings - 6th European Microwave Integrated Circuit Conference, EuMIC 2011*, Manchester, UK: IEEE, 2011, pp. 348–351, ISBN: 9782874870231.
- [14] *2 - 6 GHz GaN Low Noise Amplifier*, TGA2611, Rev. 01-29-15, Qorvo, Jan. 2015.